Semiconductor Optoelectronics
ISSN: 1001-5868

UV LIGHT-ASSISTED PHOTODEGRADATION OF INDUSTRIAL DYES BY GRAPHENE/MAGNESIUM-CODOPED FE_3O_4 NANOCOMPOSITES SYNTHESIZED USING THE COPRECIPITATION METHOD

J.F.Joe Sherin[a], G.Edwin Sheela[a*]

[a]Research Scholar (Register No. 20113232132005), Department of Physics, Muslim Arts College, Thiruvithancode-629174, Affiliated to Manonmanium Sundaranar University, Abishekapatti, Tirunelveli-627 012, Tamilnadu, India.
sherinjfjs@gmail.com

[a*]Department of Physics, Muslim Arts College, Thiruvithancode, Kanyakumari District-629174, Tamilnadu, India.
sheelalivings@gmail.com

Abstract

Waste from industrial dye production is extremely hazardous, nonbiodegradable and has a detrimental environmental impact. Photodegradation of phenothiazine derivative dyes by undoped Fe_3O_4 nanoparticles (F-NPs), graphene -doped Fe_3O_4 nanocomposites (G/F-NCs), magnesium-doped Fe_3O_4 nanoparticles (Mg/F-NPs) and graphene–magnesium codoped Fe_3O_4 nanocomposites (G/Mg/F-NCs) utilises a simple coprecipitation process to obtain. All of the prepared samples' X-ray powder diffraction patterns support the face-centered cubic structure of metallic Fe_3O_4. The Mg-doped samples show an increase in crystallite size, showing that the addition of Mg 2s considerably accelerates the formation of crystalline grains in Fe_3O_4, in contrast to the addition of graphene dopants, which results in a decrease in particle size and an expansion of the bandgap. Due to the addition of graphene nanoflakes and the development of secondary pores, G/Mg/F-NCs have a larger specific surface area (82.533m^2/g). The presence of oxygen anions, graphene, Mg 2s ions, and the Fe_3 and Fe_2 oxidation states in the Fe_3O_4 lattice is verified by the X-ray photoelectron spectra of O 1s, C1s, Mg 2s, and Fe 2p.

Keywords: graphene-magnesium codoped Fe_3O_4 nanocomposites; XRD; XPS; EDAX

1. Introduction

The two most important problems facing the globe now are environmental pollution and the energy crisis. One of the biggest problems facing the energy storage sector is the production of energy from inexpensive materials. As opposed to that, industrial water pollution is a significant environmental issue. Xenobiotic composites (dyes) make up a significant portion of industrial waste in developed nations. These are harmful to humans, animals, and aquatic organisms and difficult to biodegrade (VanHuyNguyen et al., 2020). The existence of nitrogen and sulphur in the thyazine dyes results within heterocyclic series. Particularly, Methylene Blue (MB) is a thyazine dye (medicine dye) that is frequently found in industrial waste-water and is taken into consideration in the current instance due to a major side effect and negative environmental effects (Chandra et al., 2010). Degrading water using industrial

dye inexpensive along with environmentally acceptable materials is crucial. Magnetite (Fe_3O_4) nanoparticles have generated a great deal of interest in the research community over the past few years due to their diverse physicochemical features. For their great oxidative stability, biocompatibility, chemical strength and magnetic properties magnetic iron oxide nanoparticles are a subject of much research. Fe_3O_4 nanoparticles have been used extensively in a variety of applications, including MRI contrast agents, metal ion absorbents in water treatment, hyperthermia therapy, drug delivery, cancer diagnosis, photomagnetic imaging, the fabrication of supercapacitor devices, photocatalysis, sensors, and more (Beji et al.,2010; Kim et al., 2010; Gautam et al., 2017; Liu et al., 2020; Bharath et al., 2022; Kim et al., 2005; Dubus et al., 2006; Chang et al., 2005; Setiadi et al., 2017).

One of the most magnetic nanoparticles is Fe_3O_4 (magnetite). A ferrimagnetic oxide with a cubic inverse spinel structure, Fe_3O_4, has been the subject of much research. Iron sand primarily contains Fe_3O_4 as a mineral (Jalil et al., 2017; Riana et al., 2018). Due to the electron hopping between the Fe^{2+} and Fe^{3+} ions in the octahedral locations, it demonstrates magnetic and electric characteristics. It is well known that transition metal ions can be added to Fe_3O_4 to increase its catalytic activity (Mahdavi et al., 2013). Doping Fe_3O_4 with rare earth or transition metal elements can enhance the magnetic properties of the material (Tsai et al., 2004; Chen et al., 2005; Penc et al., 1999; Li et al., 2004). The structural, magnetic, and transport properties of the related magnetite-based materials are frequently altered by the doping of Fe_3O_4 in thin film samples (Takaobushi et al., 2007; Tripathy et al., 2007; He et al., 2013; Moyer et al., 2011; Chou et al., 2005). There are many ways to make magnetic Fe_3O_4 nanoparticles, including hydrothermal synthesis, thermal decomposition, micro-emulsion, co-precipitation, sol-gel, thermal treatment, solvothermal, combustion, ceramic method, soft mechanochemical method, sonochemical method, and microwave-assisted synthesis (Hong et al., 2006; Hu et al., 2006; Naseri et al., 2011; Yadav et al., 2017; Agusu et al., 2019; Lazarevic et al., 2013; Deng et al., 2005; Xu et al., 2009; Amara et al., 2009; Tang et al., 2004; Laurent et al; Hu et al., 2007; Matijevicet al., 1975).

Due to their biocompatibility and high saturation magnetization, which make them suitable for a variety of biomedical applications, Fe_3O_4 nanoparticles have been extensively researched over the past several decades (Qiao et al., 2009; Yang et al., 2009; Lu et al., 2007; Laurent et al., 2008). For the removal of arsenic in particular, the use of Fe_3O_4 for the separation of water contaminants has become established in ground water treatment. According to Deng et al. (2005), the co-precipitation approach involves a process in alkaline conditions where stoichiometric mixes of ferrous and ferric hydroxides yield large amounts of Fe_3O_4 nanoparticles. The low temperature, quick reaction time, and high reaction yield of this approach are its distinguishing features (Yang et al., 2011). Fe_3O_4 nanoparticles indicate higher SA:V with enhanced paramagnetic activity as a result. As a result, the technique of breakdown is increased by lowering the surface energy and potent dipolar attraction of nanoparticles (Liu et al., 2019). Fe_3O_4 is thus recognised is an essential substances regarding photocatalysis due to it's affordable, extremely sensitive surface, rapid electron transfer, and effective adsorption of harmful water contaminants. These properties support a suitable magnetic partition with an external magnet to process or remove nanocomposites (Balamurugan et al., 2019) (Liu et al., 2019). The surface characteristics, bonding efficiency, lattice flaws, and electronic and lattice structure of a transition metal oxide can all have a significant impact on how well it performs

as a photocatalyst (Balamurugan et al., 2019; Liu et al., 2019). Recently, cation doping into iron oxide has been widely developed to adjust the physical and chemical characteristics of Fe3O4 nanoparticles, such as the strength of the metal-oxygen bond, bulk defects, lattice structure, etc., and hence improve catalytic and energy storage performance (Liu et al., 2019; Bharath et al., 2022).

Magnesium is a low-cost, naturally abundant metal that can improve magnetite's redox stability at high temperatures (Ferreira et al., 2014). The structure, vacancies, and OSC of the final powder may significantly change when divalent cations (Mg) are included in the trivalent host structure (Fe_3O_4) (Franco et al., 2009; Nakagomi et al., 2009). Studies of the nanoparticle magnesium ferrite $MgFe_2O_4$ show that the degree of inversion depends on the synthesis method and may be modified by processing parameters (Chen et al., 1999; Da et al., 2011; Naseri et al., 2014). To our knowledge, only one study has been done on the magnesium doping of nanosized magnetite with the goal of determining if it may be used as an anode material in lithium batteries, despite the Mg^{2+} ion's promising features (Lv et al., 2019). Since magnesium (Mg) is the central atom of the chlorophyll molecule, which is responsible for energy utilisation, magnesium (Mg) is a crucial micro component for all crops to use solar energy for the photosynthesis process. Mg is also largely responsible for activating the enzymes involved in photosynthesis, respiration, and the production of nucleic acids. The first stage of plant growth, seed germination is also the most delicate stage and has a significant impact on crop output and quality (Karthikkumar et al., 2022). Due to its effective ionic radii, we chose divalent Mg^{2+} as the dopant in this work. According to Skoyszewska et al. (2003), the magnesium zinc ferrite combination is a soft ferrite.

Due to its special properties and wide range of uses as electronic components, an active ingredient in the production of supercapacitor electrodes, a component of biosensors, an adsorbent, and a medium for thermal transport, graphene is thought to be the most sought-after substance in the research sector (Balamurugan et al., 2018). Doping with graphene can improve a material's conductivity, theoretical surface area (2600 m^2/g), chemical strength, and thermal stability (Balamurugan et al., 2016; Chen et al., 2019; Vijayalakshmi et al., 2021; Vermisoglou et al., 2019; Ng et al., 2017). In order to increase the efficiency of several energy conversion, storage, and catalytic reactions, metal oxides and graphene will be coupled (Wu et al., 2010; Ashraf et al., 2021). Fe_3O_4 nanoparticles can be prepared using a wide variety of techniques, including electrospray, microemulsion, co-precipitation, hydrochemical reaction and flow injection (Liang et al., 2020; Hosseini et al., 2013; Anjana et al., 2018). Due to its low cost, environmental friendliness, exceptional product purity and yield, and reproducibility, co-precipitation processes have become one of the most popular synthesis methods (Athar et al., 2015; Cruz et al., 2018).

A single sheet of carbon atoms makes up the unique class of carbon-based nanomaterial known as graphene (G). Graphene's exceptional electric, thermal, and mechanical properties have sparked a great deal of current nanotechnology research interest (Geim et al., 2007). Based on these properties, it has an applications in many areas, such as molecular probes (Wang et al., 2010; Lin et al 2011), electrochemical sensors (Tang et al., 2009; Wang et al., 2010; Wang et al., 2012; Wang et al., 2012) nanocomposites (Wang et al., 2010; Wang et al., 2012) electronic components, adsorbents, thermal transport mediums and the active material used to make supercapacitor electrodes (Simeonidis et al., 2007; Zhou et al., 2008). Graphene may be

a better alternative as an adsorbent for the extraction of benzenoid form compounds because it has multiple delocalized-electron systems that can create a strong - stacking interaction with benzene rings (Han et al., 2012; Zhang et al., 2013; Zhao et al., 2011). It was initially obtained in a lab setting using the "scotch tape" approach (Novoselov et al., 2004). Large specific surface area, amazing mechanical rigidity, extraordinary electrical transport, and great biocompatibility are just a few of graphene's unique properties, which suggest that it is a good candidate for electrode modification (Yang et al., 2010). However, because graphene is hydrophobic, it cannot work in water. Aftabtalab et al. (2015) and Giraldo et al. (2013) found that rGO has good potential as a porous material for seawater desalination, which removes various water pollutants including metallic ions, anions, microplastics, nanoparticles, organic chemicals, and biological substrate. This technology is referred to as a "rising star" of water purification. Graphene could be transformed into graphene oxide (GO) through oxidation to enhance its dissolving characteristic (Zhao et al., 2015; Lee et al., 2015). Using reducing agents, reduced graphene oxide (rGO) is created from graphene oxide (Mussa et al., 2020). Although it resembles graphene in many ways, the surface may also include some oxygen-containing groups. According to Sharma et al. (2017), the rGO sheets are a form of chemically produced graphene.

Reactive oxygen species (ROS) produced by the surface contact-based bioactivity of graphene-based materials rendered them suitable for cytotoxicity research (Perreault et al., 2015; Gurunathan et al., 2013). In the current situation, the findings of graphene and graphene in combination with IONPs have been reported (Santos et al., 2012; Pelin et al., 2017; Hastak et al., 2018; Yang et al., 2019; Jedrzejczak et al., 2017; Gade et al., 2015). The impact of graphene with Fe_3O_4 on relative survivability and DNA integrity was examined by Jedrzejczak-Silicka et al. in 2017. They concluded that the material had high biocompatibility and mentioned that it might be used to treat hyperthermia. In order to enhance transfer and adsorption qualities, Fe_3O_4/graphene composites have attracted a lot of attention (Wang et al., 2012; Yao et al., 2012). Since the creation of a synergistic effect may be expected to have high potential in lithium ion batteries, microwave-absorbing materials, biomedicine, and supercapacitors, graphene/Fe_3O_4 composite film has received particular attention (Zhou et al., 2010; Zhang et al., 2014; Ou etval., 2014; Liu et al., 2014). Purified rGO/Fe_3O_4 nanoparticle dispersion generated by chemical reduction technique (Liang et al., 2010) to synthesise graphene-based films. Hybrid sheets of graphene and F-NP demonstrated superparamagnetic characteristics for potential use as magnetic switches. The reduced graphene oxide is in efficient electrical contact with the Fe_3O_4, helping the conductivity and preventing the loss of Fe_3O_4caused by volume changes during discharge/charge processes. (Cunqing et al., 2017) prepared Fe_3O_4/graphene nanosheet composite by hydrothermal method. As a photocatalytic material, Fe_3O_4/rGO nanocomposites can be employed (Peik et al., 2014; Padhi et al., 2017), Cu^{+2}, Zn^{+2}, and Ni^{+2} ions are among the heavy metals that can be reduced (Moradinasab et al., 2016), Cr^{-2}, Pb^{2+}Al et al. (2016), Cao et al. (2015), Wang et al. (2015), Sun et al. (2014), Cd^{+2} detection (Yu et al., 2014) ions, phenol degradation, and antimicrobial properties (Padhi et al., 2017), Yu et al. (2014) described biosensing, and Yang et al. (2015), Yang et al. (2018), Namvari et al. (2014) described absorbent for removing dyes from aqueous solutions. It could be incorporated into a sensor that looks for arsenic in mineral water (Cui et al., 2012; Chimezie et al., 2017) and the treatment of waste water (Mahalingam et al., 2018). The combination of

graphene and Fe_3O_4 offers the potential to act in a photo-Fenton-type response to provide a practical, safe, and environmentally friendly method for degrading commercial dyes.

Due to its considerable pollutant removal and conversion to unharmful byproducts (CO_2 and H_2O) during the photodegradation process, it has been utilised to treat industrial waste water (Gupta et al., 2012). Because to their high activity, stability, efficacy and lack of toxicity during prolonged use, iron oxides have been the subject of extensive research for many years (Chin et al., 2007, Mandal et al., 2015; Yavuz et al., 2006). Due to their enormous surface area ($2600m^2/g$), superior mechanical flexibility, and optical transparency, graphene functionalized nanocomposites have been shown to greatly improve the photodegradation properties (Gupta et al., 2012). Natural colours, heavy metal ions, and pesticides can all be removed by attaching graphene to the surface of river sand (Gupta et al., 2012). For the treatment of waste water, graphene-Fe_3O_4 has been found to photodegrade contaminants (Karim et al., 2022). The combination of graphene and Fe_3O_4 offers the ability to breakdown industrial dyes in a way that is efficient, nontoxic, and environmentally beneficial. Studies on the photodegradation of coloured dyes by graphene- and magnesium-doped Fe3O4 are not very thorough. As a result, it is anticipated that double doping Fe_3O_4 with both magnesium (Mg) and graphene (G) will produce better results than either doping the material with a single element or not at all. Here, the degradation of an industrial dye is evaluated using Mg and G as dopants on Fe_3O_4.

2. Experimental

2.1 Materials

The National Scientific Company in Madurai provided the ferric chloride hexahydrate ($FeCl_3.6H_2O$), ferrous chloride tetrahydrate ($FeCl_2.4H_2O$), and 30% ammonia solution (NH_3). From Sigma-Aldrich, graphene and Magnesium Nitrate $Mg(NO_3)_26H_2O$ were bought. Himedia Laboratories Pvt. Ltd. was where the washable reagents were purchased. Deionized water was used to prepare each aqueous solution. Analytical-grade ingredients were employed throughout this project without further purification.

2.2 Preparation of nanocomposites

Fe_3O_4 nanoparticles (F-NPs), graphene-doped Fe_3O_4 (G/F-NCs), magnesium-doped Fe_3O_4 (Mg/F-NPs), and graphene-magnesium codoped Fe_3O_4 (G/Mg/F-NCs) nanocomposites were all created.

Fe_3O_4 nanoparticles were made by dissolving 0.14 M $FeCl_3.6H_2O$ and 0.07 M $FeCl_2.4H_2O$ in deionized water while stirring continuously (Maity et al., 2007; Arakha et al., 2015; Ramanathan et al., 2021). Dropwise additions of the 30% ammonia solution were made to the previously obtained homogenous solution, and the temperature was held at that level for one hour while stirring continuously. Using a pH metre, the solution's pH was determined to be 7. A precipitate that was black in colour resulted from the reaction. The resulting precipitate was calcined at 300°C for one hour after being washed three times with distilled water. And F-NPs were used to identify the processed sample. The following equation can be used to talk about the complete process:

$$FeCl_2 + FeCl_3 + 8NH_3 + 4H_2O \rightarrow Fe_3O_4 + 8NH_4Cl$$

The primary homogeneous solution was supplemented with 0.05 g of graphene, and the same procedure as for the manufacture of F-NPs was followed to create the graphene doped Fe_3O_4 nanocomposite. Moreover, G/F-NCs was assigned to the prepared sample.

The primary homogeneous solution was mixed with 0.09 g of magnesium nitrate $Mg(NO_3)_26H_2O$ to create the magnesium doped Fe_3O_4 nanocomposite. Additionally, the processed sample was identified as Mg/F-NPs on the label.

The initial homogeneous solution was supplemented with 0.05 g of graphene and 0.09 g of magnesium nitrate $Mg(NO_3)_26H_2O$ to create a graphene and magnesium double doped Fe_3O_4 nanocomposite. This procedure was repeated to create F-NPs. G/Mg/F-NCs was a label applied to the prepared sample. The obtained product served as the basis for additional characterizations. Fig. 1 presents F-NPs, G/F-NCs, Mg/F-NPs and G/Mg/F-NCs are all shown schematically in the diagram.

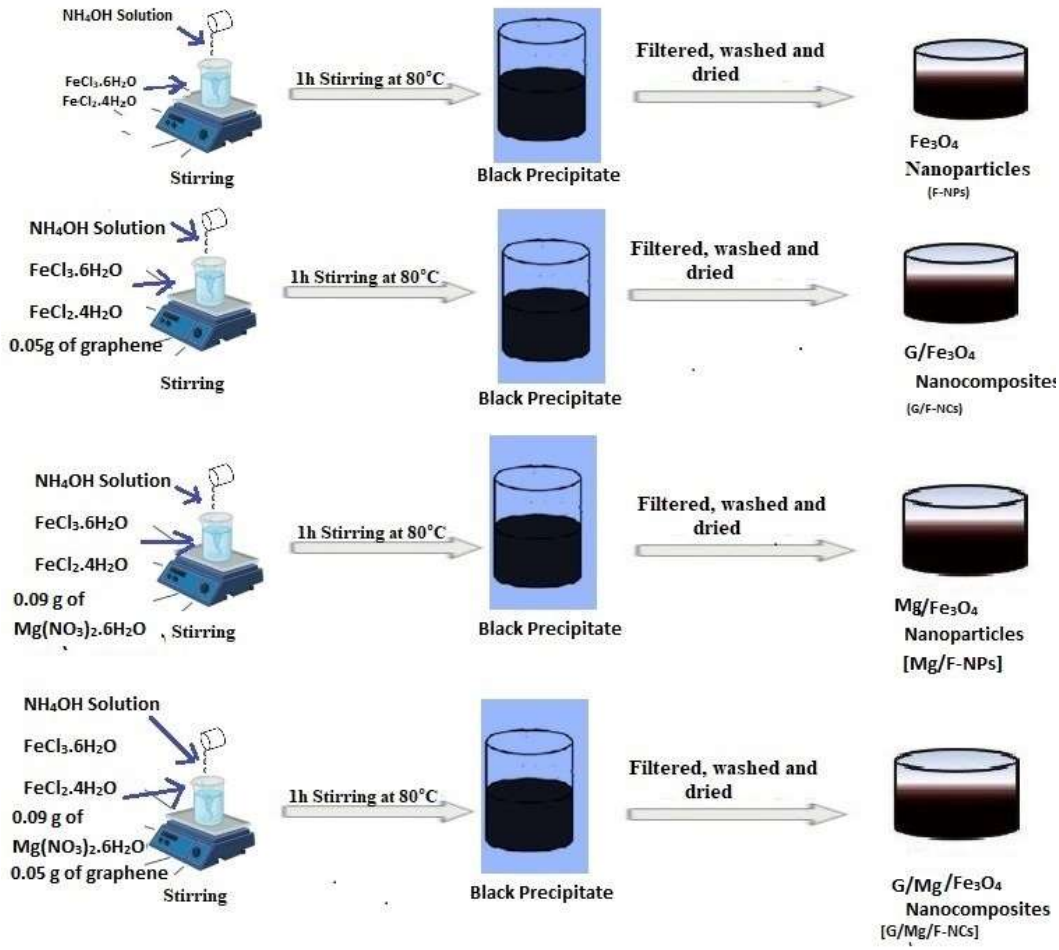

Fig. 1 shows a schematic for the production of F-NPs, G/F-NCs, Mg/F-NPs and G/Mg/F-NCs

2.3 Instrumentation

To analyse the crystal structure of the created nanomaterials, a powder X-ray diffraction setup (Philip's X'pert Pro X-ray diffractometer) outfitted with Cu K radiation (= 0.15406 nm) was utilised. Utilising a microfocused (200 m, 15 KV) monochromatic Al-K X-Ray source (hv = 1486.6 eV) mounted on a PHI 5000 Versa Probe II (purchased from ULVAC-PHI Inc., USA) X-ray photoelectron spectroscopy (XPS) studies, the oxidation states of the samples were

examined. UV-visible and photoluminescence (PL) spectroscopy are used to examine the produced nanoparticles' optical characteristics. For vibrational experiments, a Shimadzu FT-IR spectrophotometer was employed with Fourier Transform Infrared Spectroscopy (FT-IR). Using scanning electron microscopy (EOL JSM-5600 LV), the sample's surface and elemental maps were captured on film. The elemental makeup of the synthesised sample was examined using energy dispersive spectroscopy (EDAX). Using transition electron microscopy and a selected area electron diffraction pattern (SAED) (FEI, TECNAI S twin microscope with a 100 KV acceleration voltage), the material's microstructure and particle size were investigated. Brunauer Emmett Teller (BET) (Altamira Instruments, Inc.) (2 nm-500 nm, mesopore and macro porous analysis) Adsorbate: N_2, Ar Degassing temp: upto 350° C was used to examine the material's BET surface area adsorption and desorption isotherms.

The antibacterial efficacy of F-NPs, G/F-NCs, Mg/F-NPs and G/Mg/F-NCs against Pseudomonas aeruginosa and Staphylococcus aureus was assessed using the disc diffusion method. To raise the culture up to McFarland standards (108 CFC/mL), all samples were inoculated into sterile nutrient broth (Hi Media) (1.5 mL) and grown for two hours. Utilising a sterile spreader, the inocula were applied to brand-new nutrient agar plates. The selected centre received the control disc. On Mueller-Hinton-Agar/Hi Media, each unique organism appeared three times after being exposed to 100 L of revived culture. A single well with a diameter of 4 mm was used to hold all of the ready samples (50 L). All of the petri plates were kept at 37 °C for 24 hours, and the zones of inhibition (ZOI) were measured in centimetres.

Using a UV-vis spectrophotometer (Systronics 2203, India), the photocatalytic activity of F-NPs, G/F-NCs, Mg/F-NPs and G/Mg/F-NCs was evaluated. Methylene Blue (MB) dye concentration of 8 mg L^{-1} with a pH of 8 was mixed with 0.9 mg L^{-1} of an aqueous solution of the created catalysts to test the dye's degradation when exposed to UV radiation.

3. Results and Discussion

3.1 Structural Studies

Figure 2 depicts the XRD appearance of F-NPs, G/F-NCs, Mg/F-NPs and G/Mg/F-NCs. The XRD appearance of F-NPs contains indexes for the peaks of diffraction at18.46° (111), 30.25° (220), 35.64° (311), 43.01° (400), 53.78° (422), 57.16° (511) and 62.54° (440). The XRD appearance of G/F-NCs is indexed through the diffraction peaks at 18.37° (111), 30.41° (220), 35.47° (311), 43.23° (400), 53.37° (422), 56.97° (511) and 62.63° (440). When the graphene (002) peak appears in G/F-NCs, G/F-NCs nanocomposites have formed. The XRD appearance of Mg/F-NPs is indexed through the diffraction peaks at 18.39° (111), 30.23° (220), 35.41° (311), 42.25° (400), 52.28° (422), 56.32° (511) and 62.39° (440). It should be noted that the XRD pattern of spinel ferrites has a similar profile to that of cubic Fe_3O_4, with a small difference in the position of the diffraction peaks dependent on the doped ionic radii of cation in the metal oxide structure (Jeong et al., 2016; Naderi et al., 2019). As a result, when Mg cations are doped into Fe_3O_4, most of the peaks move to a lower angle due to Mg's larger atomic radius (173 pm) compared to Fe's (126 pm) (Rahmani et al., 2016). The peaks of the G/Mg/F-NCs XRD pattern are indexed at18.16° (111), 30.41° (220), 35.74° (311), 42.62° (400), 53.47° (422), 56.79° (511) and 62.46° (440). According to Cheng et al. (2017), the G/Mg/F-NCs' XRD pattern showed a tiny peak at 24.3° in agreement with graphene's (002) reflection. These findings suggest that the Fe_3O_4 crystal phase in the G/Mg/F-NCs was unaffected by the graphene addition. The Face Centred Cubic (FCC) Fe_3O_4 nanoparticles from

the JCPDS file No. 65-3107 (Anjana et al., 2018) are reflected in these images.

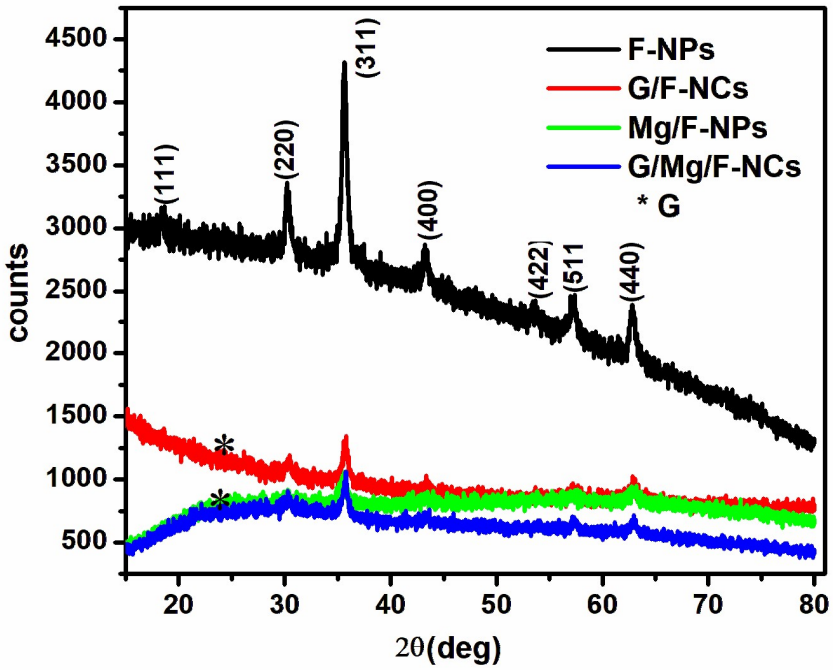

Figure 2 shows the X-ray diffraction patterns of F-NPs, G/F-NCs, Mg/F-NPs and G/Mg/F-NCs.

Table 1 lists the dislocation density of F-NPs, G/F-NPs, Mg/F-NPs and G/Mg/F-NCs as well as the crystalline size, cell volume, lattice constant, strain, bond length on the octahedral (dBx), and tetrahedral (dAx) sites of the cubic spinel structure. Scherrer's equation predicted that the crystalline diameters of F-NPs, G/F-NCs, Mg/F-NPs and G/Mg/F-NCs were, respectively, 34.22 nm, 38.61 nm, 40.35 nm, and 39.12 nm. In comparison to F-NPs, Mg/F-NPs offer bigger sizes based on predicted crystallite sizes. This shows that the addition of Mg 2s can greatly accelerate the growth of the crystalline grains in F-NPs, as indicated by the fact that the crystalline size of Mg/F-NPs increased. For F-NPs, G/F-NCs, Mg/F-NPs, and G/Mg/F-NCs, respectively, the resulting lattice parameters are determined to be around 8.3880, 8.3845, 8.3817 and 8.3829. They have a value of 8.396 and are significantly less than bulk matter. This is due to the interior atoms' compression into the spherical bodies, which led to the assemblage of nanoparticles (Sun et al., 2006). The Mg cations were also found to be more evenly distributed in the Fe_3O_4 lattice without the production of the Mg phase or its oxide, according to these data. Doping is known to have a significant impact on the physicochemical characteristics of nanoparticles, with the size (ionic radius) and redox potential of the dopant element playing the two key roles (Wang et al., 2017).The computed lattice parameter and cell volume values match those in JCPDS file no. 65-3107 well (a=8.390, V= 590.70 3). Since the values of cell volume are directly proportional to the values of lattice constant, they exhibit a similar pattern to those of the lattice constant values (Somvanshi et al., 2020). The cations at the tetrahedral and octahedral sites can be described using the variance in the I220/I440 values (Lassoued et al., 2018).

Table 1: Structural parameters of XRD analysis

Sample	Grain size (D) (nm)	Lattice parameter (a (A°)	Dislocation density (δ) (m^{-2})	Cell volume (V) ($A°)^3$	Strain	Hopping length (L_A) (A°)	Hopping length (L_B) (A°)	X-ray density (d_x) (gm / cm^3)	Tetrahedral bond length (d_{AX}) (A°)	Octahedral bond length (d_{BX}) (A°)	Surface area (m^2/g)	Pore Volume (cm^3/g)	Pore size (nm)
F-NPs	34.22	8.3880	0.00085	590.17	0.0087	3.6327	2.9660	5.2119	1.8161	2.097	48.742	0.168	13.766
G/F-NCs	38.61	8.3845	0.00069	589.43	0.00099	3.6322	2.9648	5.2185	1.8153	2.0961	69.798	0.126	7.197
Mg/F-NPs	40.35	8.3817	0.00053	581.22	0.00092	3.6313	2.9622	5.2736	1.8022	2.0929	66.695	0.222	12.900
G/Mg/F-NCs	39.12	8.3829	0.00061	582.46	0.00094	3.6317	2.9629	5.2569	1.8035	2.0943	82.533	0.259	12.575

X-ray photoelectron spectroscopy (XPS) is used to determine the oxidation states of the produced G/Mg/F-NCs. The survey spectrum of G/Mg/F-NCs is shown in Fig.3(a), confirming the presence of the elements magnesium, iron, and oxygen in the finished product. Additionally, graphene's inclusion in the synthetic material is what causes the carbon peak to occur. Atomic percentage of elements detected by XPS analysis Fe of 27.12%, O of 46.97%, C of 25.61%, Mg of 1.4%. The inset of the high-resolution XPS spectrum of Fe 2p (Fig.3(b)) depicts two large peaks caused by $2p_{3/2}$ (at approximately 711.39 eV) and $2p_{1/2}$ (at approximately 725.21 eV) (Wu et al., 2015; Zhang et al., 2016). Fe^{2+} and Fe^{3+} ion-related peaks can be seen in the deconvolution of the $2p_{3/2}$ peak at 711.05 eV and 712.98 eV, respectively. Additionally, the $2p_{1/2}$ peak's deconvolution shows the presence of two peaks caused by Fe^{2+} and Fe^{3+} ions that are present in the lattice of Fe_3O_4 (Wang et al., 2012; Chen et al., 2013). The primary peak position was identified at around 89.89 eV according to the high-resolution XPS spectrum of magnesium 2s (Fig.3(c)). According to Gholinejad et al. (2017), an XPS analysis of the Mg 2s area revealed a single peak at a position of 89.89 eV, which is in good agreement with the Mg structure. Mg is present as evidenced by the location of the Mg 2s peak, which is centred at a BE of 87.89–89.89 eV. Four peaks could be extracted from the high resolution C1s level XPS spectra (Fig. 3(d)). The sp^2 hybridised carbon found in graphene is responsible for the significant peak at 284.75 eV. According to Chang et al. (2013), the different surface

oxidation states (C-O, C=O, and O-C=O, respectively) are responsible for the peaks at 285.54, 288.62, and 293.28 eV. Three peaks are seen in the high-resolution O1s spectra (Fig. 3(e)), with the primary peak appearing at 530.38 eV and being attributed to O anions in the Fe_3O_4 lattice. The two peaks at 531.86 and 532.78 eV are a result of oxygen bonding with graphene on the surface of the composite and a Fe-OH group contaminating the Fe_3O_4 particle surface, respectively. Numerous small peaks that are largely connected to surface flaws, contaminants, and chemisorbed oxygen species may be present in the high binding energy region of the spectra. If they are there at all, as can be seen from the spectra, they are not significant enough to have an effect on the current investigation, according to Wang et al. (2012).

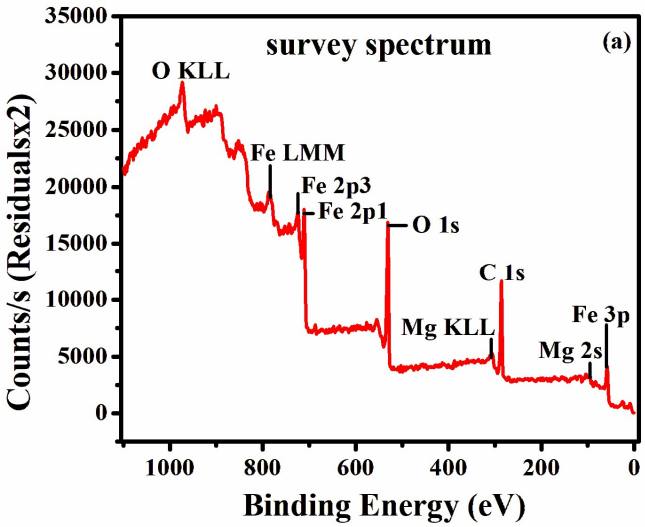

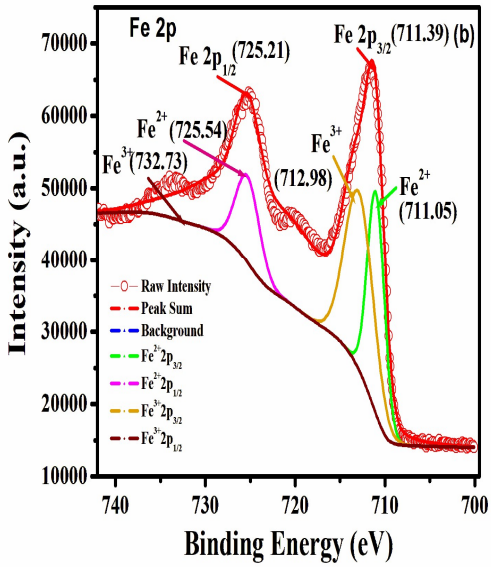

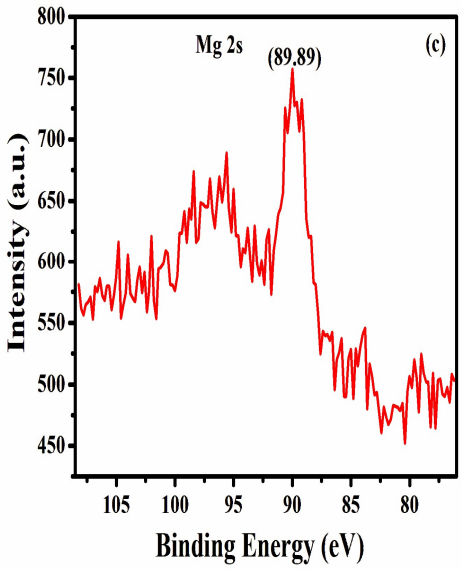

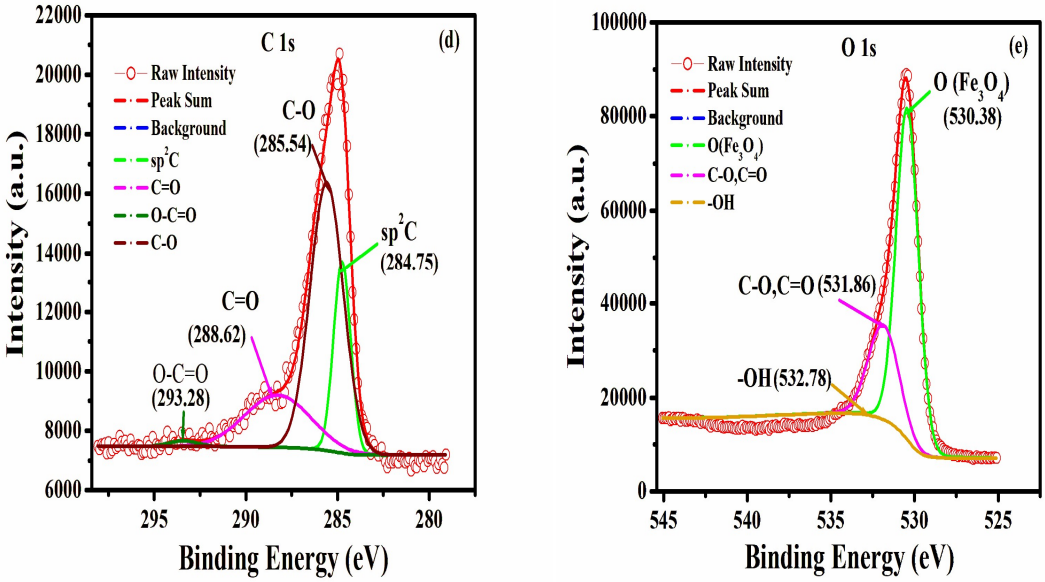

Fig.3 Synthesised G/Mg/F-NC XPS spectra: (a) The survey spectrum, (b) the Fe 2p, (c) Mg 2s, (d) C 1s, and (e) O 1s spectra

3.2 Optical studies

In Fig. 4(a) and (b), the spectra of UV-vis absorption and band gap energy map of F-NPs, G/F-NCs, Mg/F-NPs and G/Mg/F-NCs were considered in order to analyse their optical absorption and band gap properties. At 400, 405, 411, and 408 nm, respectively, optical absorption of F-NPs, G/F-NCs, Mg/F-NPs and G/Mg/F-NCs was noted. According to Fig. 4(b), the optical band gaps of F-NPs, G/F-NCs, Mg/F-NPs and G/Mg/F-NCs are 2.87, 2.65, 2.43 and 2.52 eV respectively. As is well known, a substance's band gap energy rises as the particle size falls. According to Cabot et al. (2007), the band gap of bulk Fe_3O_4 is stated to be 0.1 eV, which is less than that of the created nanocomposites. The bandgap is widened by the inclusion of Mg and G dopants. According to Anjana et al. (2018), the bandgap energies of Zn-doped Fe_3O_4 nanoparticles and undoped Fe_3O_4 nanoparticles were 2.4 and 2.25 eV, respectively. According to Anjana et al. (2023) the bandgap energies of the cobalt codoped Fe_3O_4 nanoparticles and rGO were 1.901 eV. The optical bandgaps of the rGO and nickel codoped Fe_3O_4 nanoparticles, which were identified as Fe_3O_4, Ni@Fe_3O_4, G@Fe_3O_4, and Ni/G@Fe_3O_4 (Sherin et al., 2023), were 1.970 eV, 1.824, 2.094, and 2.130 eV, respectively. It is common established that as particle size decreases, a substance's band gap energy increases (Manikandan et al., 2014; Ferraz et al., 2021). The bandgap energy fell as the particle size rose, and the optical absorption in the current instance (Mg doping) was red shifted. This could be explained by differences in the electronegativity and ionic radius of Mg and Fe caused by the formation of new defects structured as Fe atoms for Mg atoms. The system's higher disorder may be caused by the Mg 2s ions' larger ionic radius when compared to the base metal Fe_2 ions. This may potentially be the cause of the bandgap energy decline. The decrease in bandgap energy suggests that the sp-d spin-exchange interactions between the band electrons and localised d-electrons in the Mg dopants are what cause the bandgap reduction and absorption redshift (Modwi et al., 2019). The donor energy may also exceed the original valence band or the acceptor energy level may

fall below the conduction band, resulting in a decrease (Zhang et al., 2020). Mg may also induce additional impure energy in the forbidden band. The quantum confinement property of G/Mg/F-NCs is demonstrated by the high bandgap energy produced by the codoping of Mg and G into Fe_3O_4. The codopants absorbed smaller G/Mg/F-NCs more readily, which led to photocatalysis.

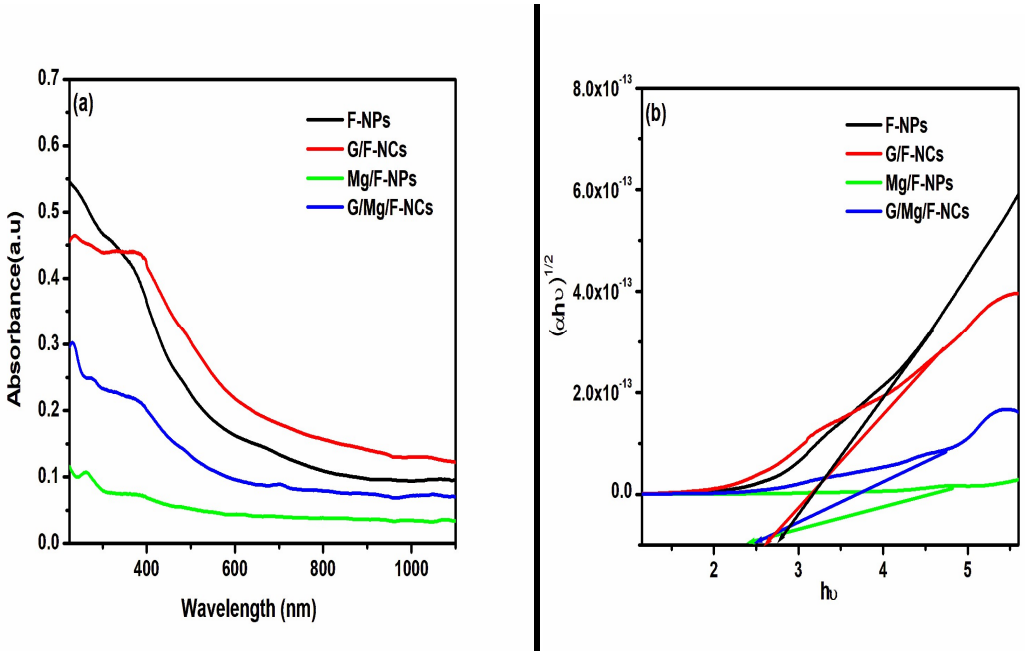

Figure 4 (a) demonstrates the UV-vis spectra and (b) shows the band gaps of F-NPs, G/F-NCs, Mg/F-NPs and G/Mg/F-NCs

By utilising photoluminescence (PL) spectroscopy, the optical characteristics of the produced nanoparticles are further investigated. The absorption of 340 nm-excited F-NPs, G/F-NCs, Mg/F-NPs and G/Mg/F-NCs is shown in Fig. 4(c). These materials exhibit PL, but at various intensities and wavelengths, from the visible to the near infrared region. F-NPs can exhibit peaks of absorption at 359.91, 492.05, 519.87, and 593.63 nm. Peaks of G/F-NCs absorption at 362.06, 493.42, 521.24, and 592.85 nm were observed. Mg/F-NPs exhibit absorption peaks at 361.38, 494.89, 535.84 and 596.38 nm. The G/Mg/F-NCs' absorption peaks may be seen at wavelengths of 361.38, 495.58, 535.15 and 596.38 nm. Bulk Fe_3O_4, however, does not demonstrate any PL. This results from the various spatial configurations and particle confinement geometries. Here, the interactions on the nanoparticle surfaces are explained by the high SA per unit mass of the nanoparticle, which increases the surface activity and tends to react with the water adsorption's hydroxide molecules. However, the Fe^{2+} ions in the Fe_3O_4 have a great affinity for connecting with water's oxygen molecules. Light stimulates semiconductor materials, causing them to produce electrons and holes. Fluorescence is produced through the recombination of electrons and holes. In order to determine the separation rate of photoinduced charges, the PL characterizations of F-NPS, G/F-NCs, Mg/F-NPs and G/Mg/F-NCs were performed. As can be shown in Fig.4(c), the PL intensity of F-NPs was considerably lower than that of G/Mg/F-NCs. The recombination efficiency of photogenerated charges in the F-NPs sample was decreased as a result of loading Fe_3O_4 (Kexin et al., 2020). The charge transfer occurring at the interface between the dopants and the oxide is what causes

graphene and bismuth doped Fe_3O_4 to glow. As a result of combined emissions and light scattering, dopants generate an excitonic emission peak that is conspicuous and red-shifted. The greater absorbance and red shift of G/Mg/F-NCs in comparison to F-NPs are attributed, according to Phan et al. (2011) and Fu et al. (2012), to the chemical bonding of the dopants with Fe_3O_4 after the addition of graphene and zinc.

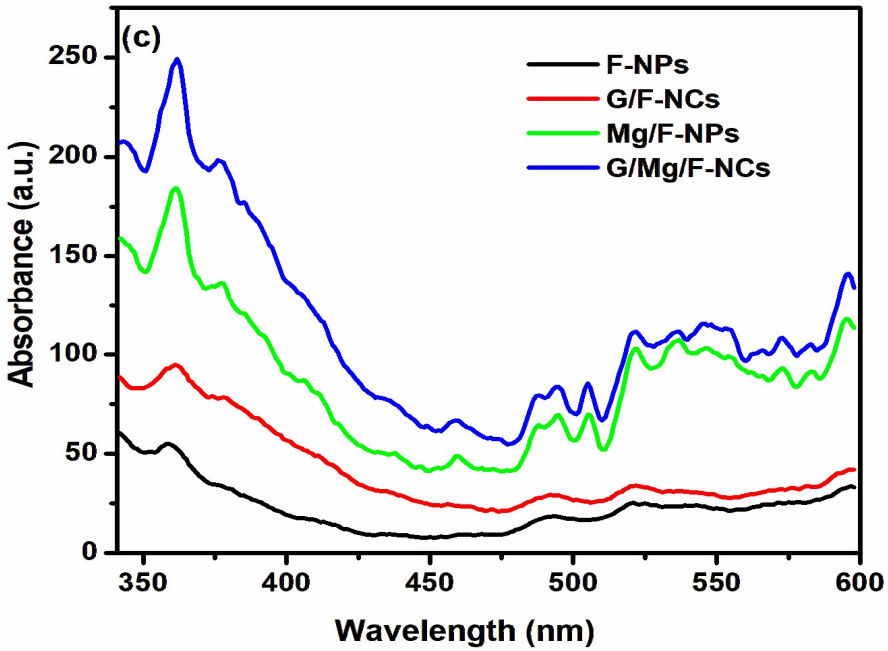

Fig. 4(c) illustrates the PL absorption spectra of F-NPs, G/F-NCs, Mg/F-NPs and G/Mg/F-NCs

3.3 Vibrational Studies

In Figure 5, the FTIR spectrum of F-NPs, G/F-NCs, Mg/F-NPs and G/Mg/F-NCs are displayed. Identifiable peaks were seen in the spectra at 3436.03, 2920.09, 2877.26, 1634.12, 1390.31, 1196.28, 1040.43, 826.64, 543.17, and 447.03cm^{-1}. The water molecules' O-H vibrations on the nanoparticles' surface are responsible for the broad bands at 3436.03cm^{-1} (Haw et al., 2011). According to Haw et al. (2011), the bands at 1634.13, 1390.25cm^{-1}, and 800.51 cm^{-1} correspond to the stretching vibrations of C=O, C-C, and C-H. Graphene is present in the samples G/F-NCs and G/Mg/F-NCs is confirmed by the presence of and C=O groups. And these weaker carbon bonding vibrations are indicated by these lowered vibrations (Rezapour et al., 2018; Lyubutin et al., 2018; Sharma et al., 2017). This is because Fe^{3+} and Fe^{2+} ions from Fe_3O_4 exist. According to Liu et al. (2018), the nanocomposite's C-N stretching vibration is what causes the peaks seen from 1235.32 to 914.86 cm^{-1}. The FTIR spectrum of G/F-NCs show a vibrational signal at about 1157.47 cm^{-1}, which is related to the stretching vibrations of the C-O and reveals the integration of graphene with Fe_3O_4 nanoparticle. The lines at 788.52, 544.84, and 447.10 cm^{-1} in the FTIR spectrum of F-NPs correspond to the Fe^{2+} and Fe^{3+} ion stretching vibrations in the octahedral and tetrahedral locations, respectively. This verifies the creation of the Fe_3O_4 spinel structure (Agnihotri et al., 2020; Keiser et al., 1982).

The bands at 788.52, 544.84, and 447.10 cm^{-1} in the FTIR spectrum of G/Mg/F-NCs have been moved towards 797.11, 563.91, and 456.41 cm^{-1}. The band's shifting was attributed up to the bond length substitution due to the Fe^{2+} ions in the Fe_3O_4 lattice were switched out for Mg ions (Yang et al., 2009). The FTIR data shows that bismuth ions were successfully incorporated into the Fe_3O_4 lattice in G/Mg/F-NCs.

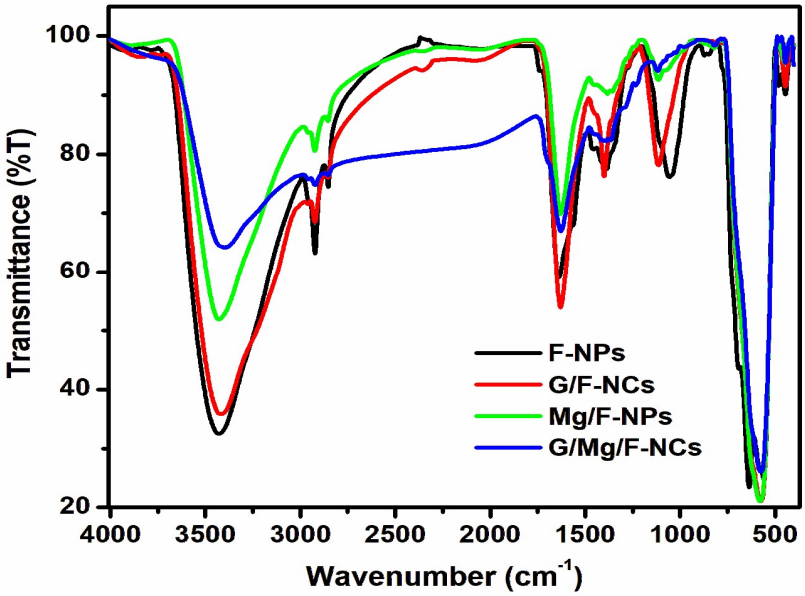

Figure 5 displays the FT-IR spectrum of F-NPs, G/F-NCs, Mg/F-NPs and G/Mg/F-NCs

3.4 Morphological studies

The synthesised materials' surface morphology F-NPs, G/F-NCs, Mg/F-NPs and G/Mg/F-NCs as determined by SEM examination is shown in Fig. 6(a), (b), (c) and (d). It is discovered that the generated nanoparticles are spherical in shape. EDAX measurement is used to assess The atomic structure of the synthesised F-NPs, G/F-NCs, Mg/F-NPs and G/Mg/F-NCs, which is shown in Fig.6(e, f, g and h). Iron signals can be seen in the EDAX spectra for all samples (F-NPs, G/F-NCs, Mg/F-NPs and G/Mg/F-NCs). The presence of oxygen in the synthesised nanoparticles is confirmed by the observation of an oxygen signal at 0.5 keV. Large peaks of Fe and O are visible in the EDAX spectra, supporting the formation of Fe_3O_4 nanoparticles. The presence of graphene in the synthesised material is shown by the carbon peak at 0.3 keV in the EDAX spectra of G/F-NCs and G/Mg/F-NCs. The EDAX spectra of G/Mg/F-NCs(Fig. 6(h))shows signals for magnesium at 1.59 keV, which is consistent with Mg present in the Fe_3O_4 nanoparticles (Mishra et al., 2016). Table 2 provides a summary of the atomic percentages of the elements found using EDAX analysis.

(a) **(b)** **(c)** **(d)**

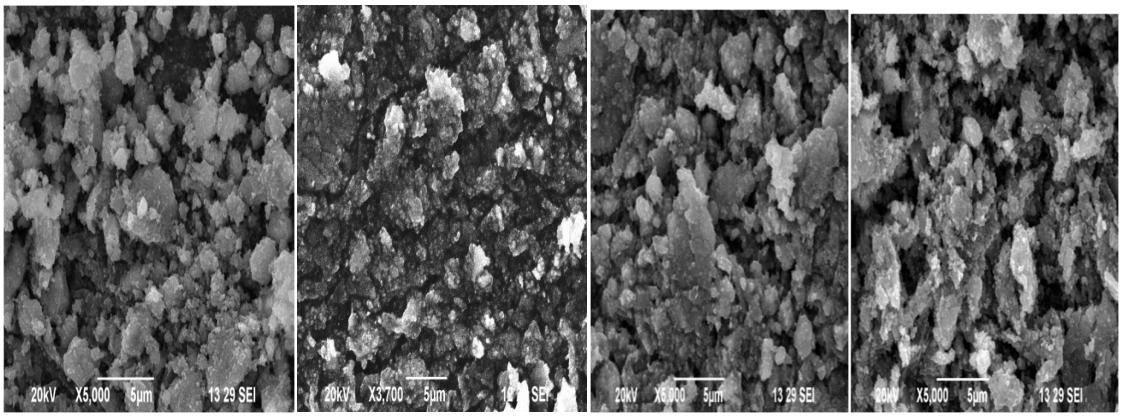

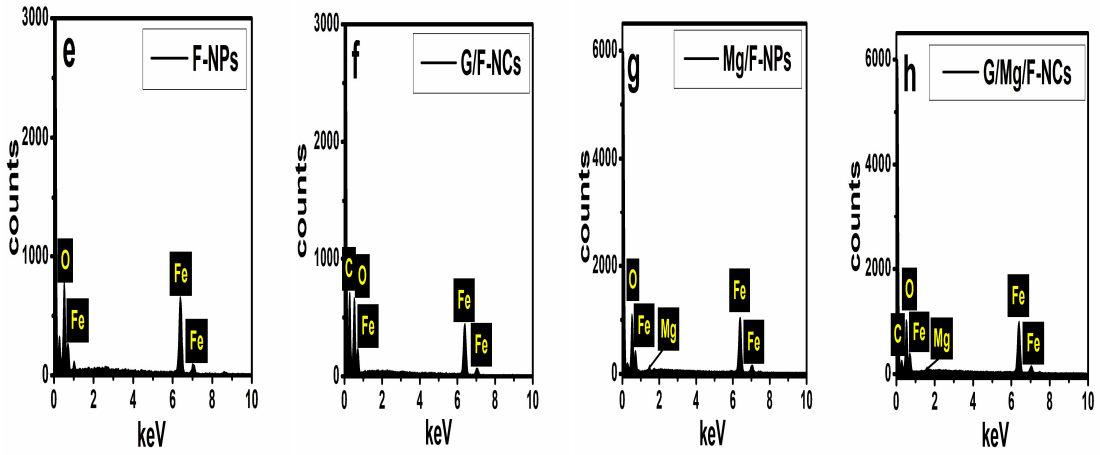

Figure 6 shows SEM pictures of (a) F-NPs, (b) G/F-NCs, (c) Mg/F-NPs and (d) G/Mg/F-NCs, together with EDAX spectra of (e) F-NPs, (f) G/F-NCs, (g) Mg/F-NPs and (h) G/Mg/F-NCs

Table.2 Atomic percentage of elements detected by EDX analysis

Samples/Element	Fe		O		C		Mg	
	(wt.%)	(at.%)	(wt.%)	(at.%)	(wt.%)	(at.%)	(wt.%)	(at.%)
F-NPs	60.48	30.48	39.52	69.52	-	-	-	-
G/F-NCs	22.55	6.69	39.54	40.98	37.91	52.33	-	-
Mg/F-NPs	58.13	29.54	38.37	70.41			5.61	1.47
G/Mg/F-NCs	59.26	29.85	34.61	58.17	6.39	13.12	0.07	0.05

TEM analysis of the microstructure of the samples of F-NPs, G/F-NCs, Mg/F-NPs and G/Mg/F-NCs is shown in Fig. 7(a), (b), (c) and (d). The produced Fe_3O_4 nanoparticles' crystalline nature is confirmed by Fig. 7. The TEM images in Figure 7(b and d) show scattered Fe_3O_4 nanoparticles on the graphene surface. F-NPs and Mg/F-NPs had computed average particle sizes of 35.72 and 40.91 nm, respectively. Furthermore, the average particle sizes for G/F-NCs and G/Mg/F-NCs were determined to be 39.14 and 39.65 nm, respectively. The slight rise average size of the particle is brought on by the chemical reaction's aggregation of

graphene. The typical crystal size estimated data from XRD is rather close to this value. Iron oxide nanoparticles have a more spherical and uniform particle dispersion when C and Mg are added. Figure 7(e, f, g and, h) depicts SAED is a pattern of F-NPs, G/F-NCs, Mg/F-NPs and G/Mg/F-NCs. All F-NPs, G/F-NCs, Mg/F-NPs and G/Mg/F-NCs exhibit rings in the SAED pattern that are connected to the (111), (220), (311), (400), (422), (511) and (440) planes and are produced as nanoparticles of iron oxide. SAED designs are all seen to be extremely intense, which proves that nanoparticle manufacturing is taking place. Because there are no additional iron salts present, the SAED pattern indicates the presence of Fe_3O_4 nanoparticles in their pure form (Sun et al., 2011).

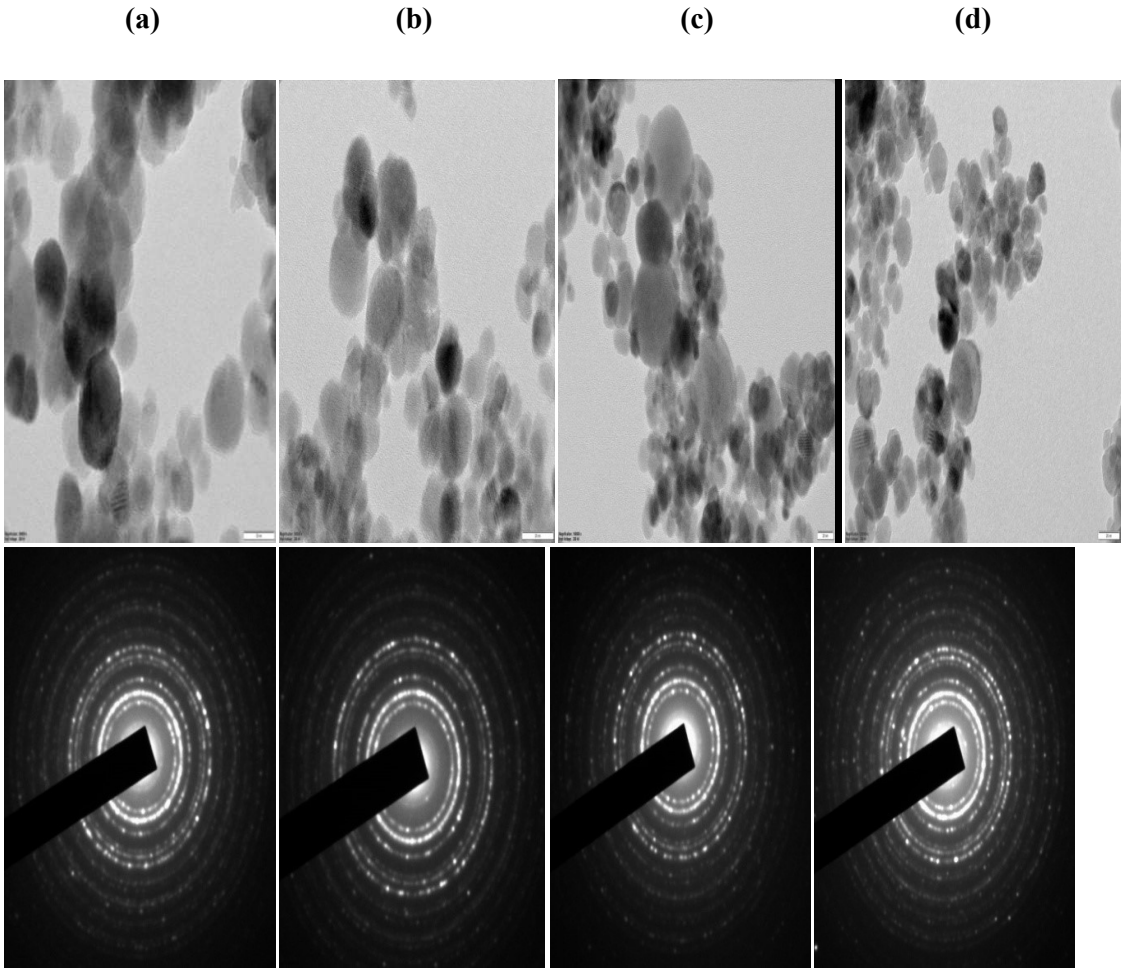

Figure 7 shows TEM images of (a) F-NPs, (b) G/F-NCs, (c) Mg/F-NPs and (d) G/Mg/F-NCs, as well as SAED patterns of (e) F-NPs, (f) G/F-NCs, (g) Mg/F-NPs and (h) G/Mg/F-NCs

3.5 BET surface area analysis

Figure 8 depicts the nitrogen-adsorption and -desorption isotherms for the samples F-NPs, G/F-NCs, Mg/F-NPs, and G/Mg/F-NCs. In Table 1, the prepared materials' surface areas, pore volumes, and pore diameters are presented. Indicating the presence of mesoporous

nanocomposites, the isotherms show significant hysteresis loops at relative pressures between 0.4 and 1. The surface areas of F-NPs, G/F-NCs, Mg/F-NPs and G/Mg/F-NCs were determined to be 48.742, 69.798, 66.695 and 82.533m^2/g, respectively, using the Brunauer-Emmett-Teller (BET) method. After Mg and G doping, the samples' increased surface area can be attributed to a reduction in the Fe_3O_4 nanoparticles' crystalline size. The enhanced specific surface area of G/Mg/F-NCs is caused by the development of secondary pores and the integration of graphene nanoflakes (Su et al., 2011; Lian et al., 2010; Chen et al., 2011). Therefore, the system with maximum surface area G/Mg/F-NCs is favorable for adsorption applications and has been chosen for further studies, i.e. adsorption of MB from wastewater (Aashima et al., 2019).

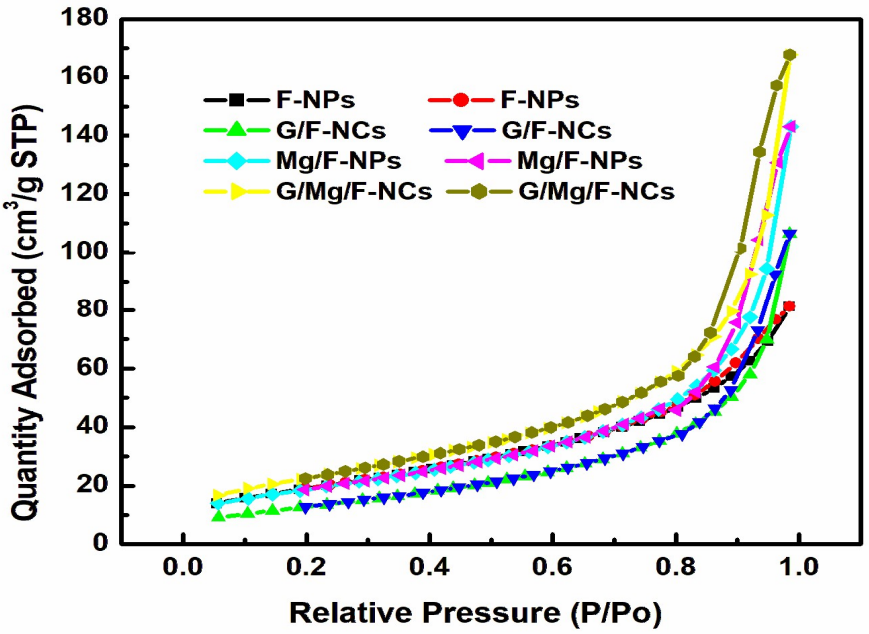

Fig.8. The isotherms of F-NPs, G/F-NCs, Mg/F-NPs and G/Mg/F-NCs for the adsorption and desorption of nitrogen

3.6 Antimicrobial activities of F-NPs, G/F-NCs, Mg/F-NPs and G/Mg/F-NCs

Despite spreading and causing a number of dangerous infections, Staphylococcus aureus is effectively contained in hospital implants (Ribeiro et al., 2012). Especially among those with weakened immune systems, Pseudomonas aeruginosa is a prevalent environmental bacterium that can infect individuals and cause a number of acute and chronic illnesses that can be fatal (Qin et al., 2022). One of the main causes of the rise in death rates is the spread of microbes that are resistant to therapy. Finding novel methods for creating medications that are effective against these bacterial strains is therefore strongly advised. The antibacterial effects of F-NPs, G/F-NCs, Mg/F-NPs and G/Mg/F-NCs on a variety of harmful bacteria, including the frequently encountered water-borne gram-positive pathogen S. aureus and gram-negative pathogen P. aeruginosa, and fungi, Aspergillus flavus, were examined using the disc diffusion method (Figure 9 and dates are listed in Table 3). Fig. 9 shows that the produced nanoparticles exhibited a maximal zone of inhibition (ZOI) of 23 mm for S. aureus and ZOIs of 20 and 21 mm for A. flavus and P. aeruginosa.

Staphylococcus aureus germs were shown to be more sensitive to chemical stressors than the other two species due to changes in the structure of their cell walls. The cell membrane of S. aureus reacts when nanoparticles come into touch with it, allowing additional metal ions to pass through. S. aureus experiences cell death as a result, which reduces its susceptibility to treatment. Due to the toxicity, oxidative stress, and electron transport of graphene, the G/Mg/F-NCs nanocomposites exhibit a substantial antibacterial activity (Kumar et al., 2019). By cutting into bacterial membranes with its pointed edges, it can cause direct damage to them. Reactive oxygen species (ROS) such superoxide and hydroxyl radicals, singlet oxygen, and hydrogen peroxide produced by graphene allow bacteria to multiply by deactivating their lipids and proteins (Kumar et al., 2019). According to Kumar et al. (2019), it serves as an electron acceptor and removes es from the membrane, potentially improving the membrane's integrity. The generation of ROS by the Fenton reaction results in lipid peroxidation, DNA damage, and protein oxidation. ROS has the ability to destroy bacteria without harming non-bacterial species. The bactericidal effects of the ROS production were applied to both good and harmful bacteria. According to Kim et al., hydrogen peroxide is created when Fe_2 reacts with oxygen. Hydroxyl radicals can harm biological molecules as a result of the Fenton reaction that occurs when the resultant hydrogen peroxide combines with ferrous ions (Kumar et al., 2019).

Fig.9 shows ZOI of F-NPs, G/F-NCs, Mg/F-NPs and G/Mg/F-NCs for Pseudomonas aeruginosa, Staph aureus and Aspergillus flaves

Table 3 ZOI of F-NPs, G/F-NCs, Mg/F-NPs and G/Mg/F-NCs

	F-NPs	G/F-NCs	Mg/F-NPs	G/Mg/F-NCs	Control (Amikacin)
Pseudomonas aeruginosa	15 mm	17 mm	19 mm	21mm	16 mm
Staph aureus	14 mm	16 mm	18 mm	23mm	15 mm
					Control (Nystatin)
Aspergillus Flaves	17 mm	19 mm	20 mm	20mm	17mm

3.7 Photocatalytic degradation of F-NPs, G/F-NCs, Mg/F-NPs and G/Mg/F-NCs

Due to its ability to oxidise harmful contaminants into minute molecular inorganic materials (CO_2 and H_2O) under the influence of light, photocatalytic degradation is one of the

most essential and effective methods for treating industrial waste water (Arefeh et al., 2019; Su shiung et al., 2020). Industrial dyeing wastes are not biodegradable, exceedingly hazardous, and have a negative impact on the environment. Methylene Blue (MB), a phenothiazine derivative used in the textile dyeing process, is exceedingly toxic and carcinogenic. In this study, we examined the photocatalytic degradation of aqueous MB caused by UV light irradiation at various time intervals in the presence of produced nanocatalysts (F-NPs, G/F-NCs, Mg/F-NPs and G/Mg/F-NCs). Fig.10(a-d) depicts the degradation of MB by photocatalysis over F-NPs, G/F-NCs, Mg/F-NPs and G/Mg/F-NCs. It demonstrated a gradual decrease in the amount of MB that was absorbed at 661 nm after 330 minutes of exposure, confirming that MB was degraded by adhering to the surface of the produced nanocatalysts.

Photons can be efficiently absorbed due to the UV region's significant absorption by nanocomposite materials. The electrons on the surface of Fe_3O_4 are moved from graphene's valence band to its conduction band. These trapped electrons produce the super oxide radical O_2 and contribute to electron hole separation while being trapped on the graphene surface. The electron-hole pairs recombination in Fe_3O_4 was controlled by the increased electrical conductivity of graphene, which began with sp^2 hybridization was restored throughout the reduction process. According to Hisatomi et al. (2014) and Hoffmann et al. (1995), the redox interaction between the MB molecules and catalyst is brought on by the electron-hole pairs. The holes on the Fe_3O_4 (photo produced) react with water, OH, and MB dye to produce hydroxyl free radicals, which are the active ingredients. The valence band's capacity to produce hydroxyl radicals and the conduction band's capacity to decrease molten oxygen are both positive at the nanoparticle surface. The organic dyes on the G/Zn/F-NCs' surface are affected by the produced hydroxyl radicals, which act as oxidising agents.

$$H\nu + Fe_3O_4 \rightarrow h^+_{vb} + e^-_{cb}$$
$$(O_2)_{ads} + e^-_{cb} \rightarrow {}^{\cdot}O_2^-$$
$$h^+ + H_2O \rightarrow H^+ + OH^{\cdot}$$

However, when they interact with H^+, the super oxide radicals produce $HO_2^{\cdot}$, which they no longer contribute to oxidation. As a result, $HO_2^{\cdot}$ radicals that have More trapped e- at the valence band combines with water and dyes to form hydroxyl free radicals, which are the active ingredients in many spices. According to Behnam et al. (2021) these radicals are created by the photocatalytic oxidation of water and the reduction of oxygen on photocatalyst surfaces.

$$^{\cdot} H^+ + O_2^- \rightarrow HO_2^{\cdot}$$
$$e^- + HO_2^{\cdot} \rightarrow OH^{\cdot}$$

As a result, MB is broken down into degradation products including CO_2 and H_2O by the radicals O_2, HO_2, and OH•.

$$OH^{\cdot} / HO_2^{\cdot} / O_2^- + MB \rightarrow \text{Degradation Products}$$

It was found that within 330 minutes of irradiation, F-NPs, G/F-NCs, Mg/F-NPs and G/Mg/F-NCs offer 62%, 71%, 51%, and 92% of MB pollutant degradation, respectively. G/Mg/F-NCs have a higher degrading efficiency than F-NPs, G/F-NCs and Mg/F-NPs. According to Asha et al. (2021; Bessy et al., 2022; Ancy et al., 2021; Bindhu et al., 2021), a linear plot of ln (At/A0) and time is shown in Fig.10(e), which shows how the rate constant (ka_{pp}) of this catalytic process was calculated using a pseudo-first-order kinetic equation. For F-NPs, G/F-NCs, Mg/F-NPs and G/Mg/F-NCs, the values of k_{app} were reported as 0.005, 0.007, 0.001, and 0.014/min, respectively. Due to both its high capacity for adsorption (produced by the number

of additional active sites for the adsorption of MB molecules on its surface) and great light diffusion, which produces high photoactivity, G/Mg/F-NCs have a predicted k_{app} value that is greater. Due to graphene's high electrical conductivity and vast surface area, G/Mg/F-NCs can increase photocatalytic activity. This improves the exchange of electrons, hydroxyl radicals, and reactive sites between the dye molecules and the catalyst. The MB's thiazine ring has a higher photoreduction susceptibility and serves as a photocatalyst sensitizer (Hoffmann et al., 1995).

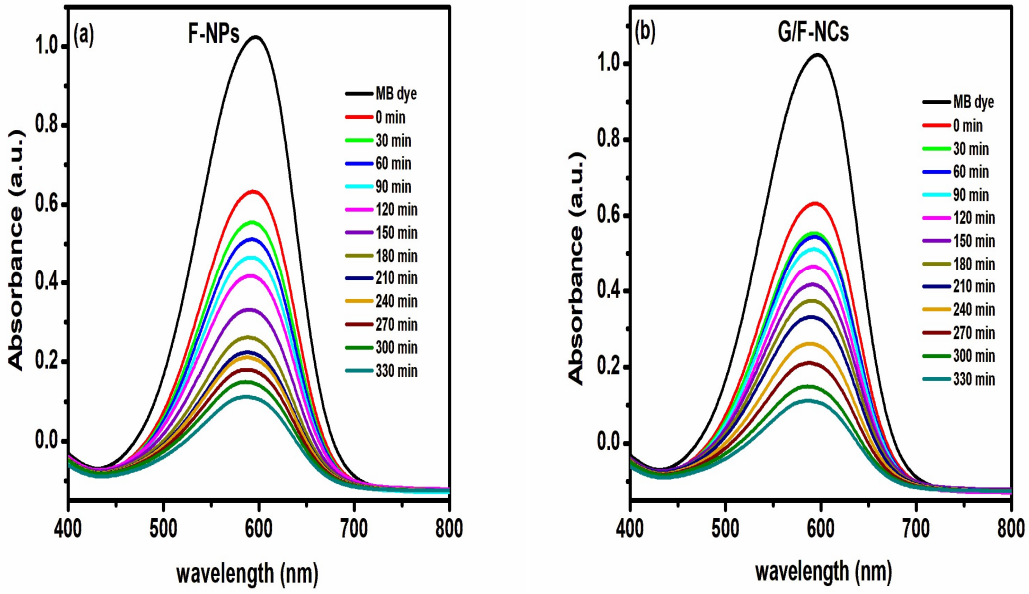

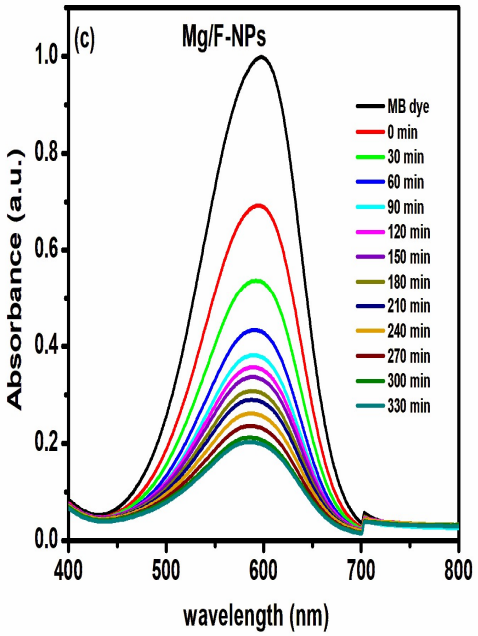
(c)
Mg/F-NPs
Absorbance (a.u.)
wavelength (nm)
MB dye
0 min
30 min
60 min
90 min
120 min
150 min
180 min
210 min
240 min
270 min
300 min
330 min

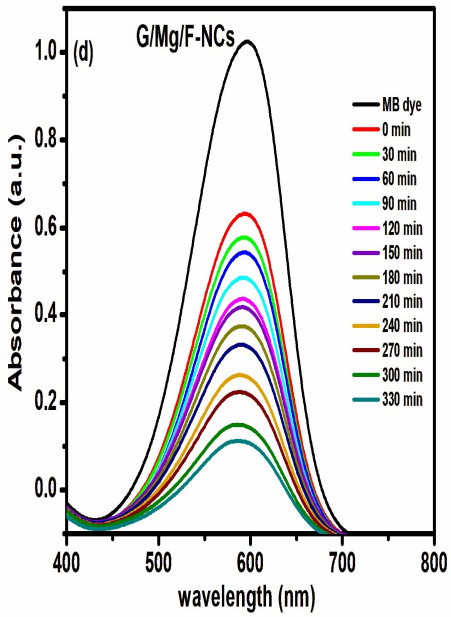
(d)
G/Mg/F-NCs
Absorbance (a.u.)
wavelength (nm)
MB dye
0 min
30 min
60 min
90 min
120 min
150 min
180 min
210 min
240 min
270 min
300 min
330 min

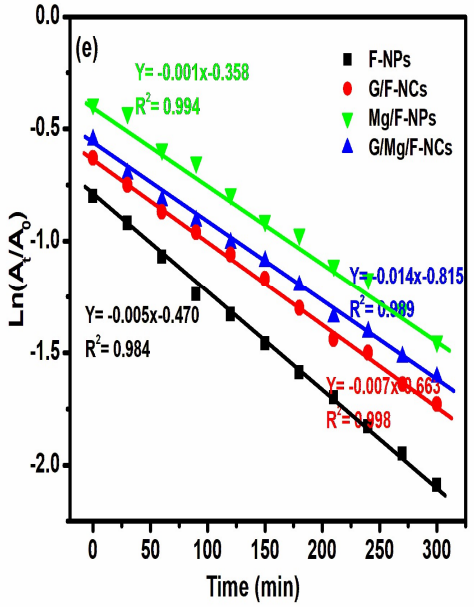
(e)
Y= -0.001x-0.358
R2= 0.994
Y= -0.014x-0.815
R2= 0.989
Y= -0.005x-0.470
R2= 0.984
Y= -0.007x-0.663
R2= 0.998
F-NPs
G/F-NCs
Mg/F-NPs
G/Mg/F-NCs
Ln(At/Ao)
Time (min)

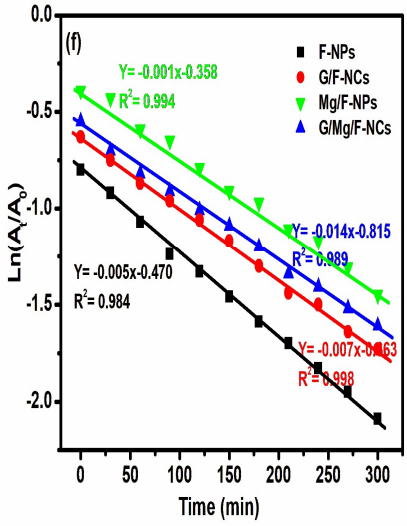
(f)
Y= -0.001x-0.358
R2= 0.994
Y= -0.014x-0.815
R2= 0.989
Y= -0.005x-0.470
R2= 0.984
Y= -0.007x-0.663
R2= 0.998
F-NPs
G/F-NCs
Mg/F-NPs
G/Mg/F-NCs
Ln(At/Ao)
Time (min)

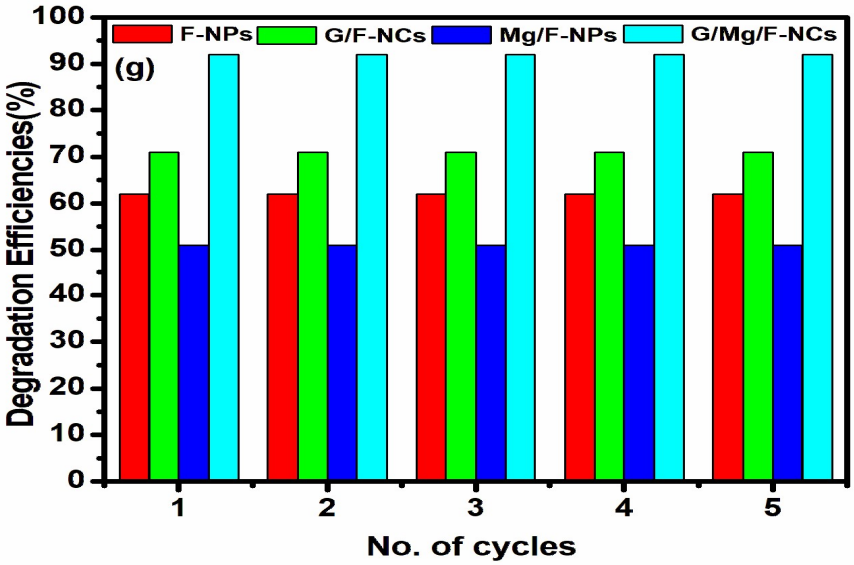

Fig.10(a-d) shows photocatalytic degradation curves of MB, (e) a linear plot of Ln (A_t/A_0) versus reaction time, (f) a linear plot of Ln (A_t/A_0) versus reaction time after seven days, and (g) degradation (%) versus number of cycles for F-NPs, G/F-NCs, Mg/F-NPs and G/Mg/F-NCs

F-NPs, G/F-NCs, Mg/F-NPs and G/Mg/F-NCs have great stability towards photocatalytic reaction, which is supported by the observation of no appreciable changes in their rate constants even after seven days (Fig.10(f)). Centrifugation is used to remove every manufactured photocatalyst by-product of the reaction mixture. It is an experiment carried out five times using photocatalysts for a comparable 330-minute reaction period. According to Fig. 10(g), there have been no appreciable modifications to degradation efficiencies. The samples calcined at 300°C as a result. This might be eliminating the contaminants that could potentially render the photocatalyst inactive. As a result, the steady catalytic activity for the photocatalysts that were regenerated (F-NPs, G/F-NCs, Mg/F-NPs and G/Mg/F-NCs) that were used to degrade MB were observed. The mechanism for the G/Mg/F-NCs' breakdown of MB dye is schematically depicted in Fig. 11.

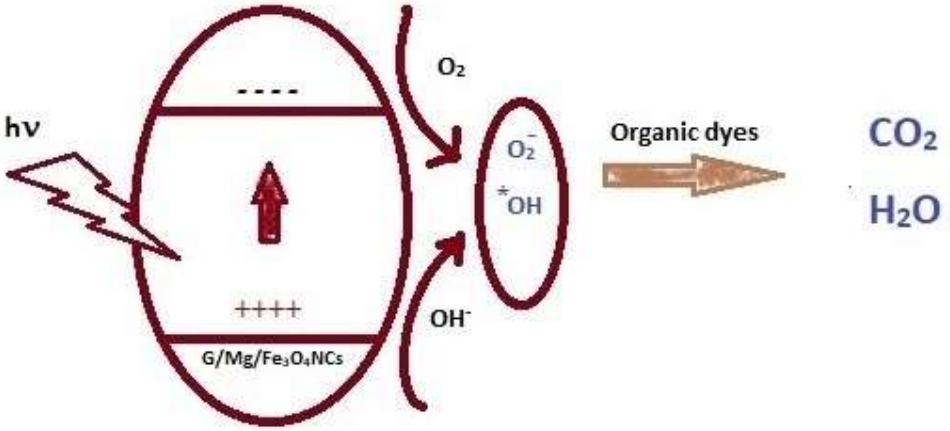

Figure 11. Schematic representation of the process by which G/Mg/F-NCs degrade MB dye

4. Conclusion

To examine the degradation of commercial dyes, the photocatalytic and antibacterial capabilities of Fe_3O_4 nanocomposites (F-NPs, G/F-NCs, Mg/F-NPs and G/Mg/F-NCs) with various levels of doping were investigated. The XRD, XPS, FTIR and EDAX results successfully showed that G and Mg 2s ions were integrated into Fe_3O_4. Scherrer's equation predicted that the crystallite sizes of F-NPs, G/F-NCs, Mg/F-NPs and G/Mg/F-NCs were, respectively, 34.22 nm, 38.61 nm, 40.35 nm, and 39.12 nm. F-NPs, G/F-NCs, Mg/F-NPs and G/Mg/F-NCs all had optical bandgaps that were, respectively, 2.87, 2.65, 2.43, and 2.52 eV. BET surface areas of 48.742, 69.798, 66.695 and 82.533 m^2/g were discovered for F-NPs, G/F-NCs, Mg/F-NPs and G/Mg/F-NCs, respectively. 0.005, 0.007, 0.001, and 0.014/min, respectively, were the computed k_{app} values for F-NPs, G/F-NCs, Mg/F-NPs and G/Mg/F-NCs. Because G/Zn/F-NCs have great photoactivity, they have a large capacity for light absorption and light diffusion, hence the expected k_{app} value was higher. The generated nanoparticles showed a maximum ZOI of 23 mm with regard to S. aureus. To improve the composite's electrical conductivity, catalytic performance, and antibacterial qualities, double dopants were added. This raised the specific surface area and improved electron conduction between the parts. We demonstrated that magnesium and graphene nanocomposites are likely to improve the binding of nanoparticles to bacteria.

5. List of abbreviations

Fe_3O_4	iron oxide nanoparticles
Mg	Magnesium
G	Graphene
F-NPs	nanoparticles of Fe_3O_4
G/F- NCs	Graphene-doped nanocomposites of Fe_3O_4
G/Mg/F-NCs	Iron oxide nanocomposites co-doped with magnesium and graphene
XRD	X-ray diffraction
XPS	X-ray photoelectron spectroscopy
FTIR	Fourier transform - infra red spectroscopy
UV-vis	UV-visible spectroscopy
PL	Photoluminescence spectroscopy
TEM	Transmission electron microscopy
SEM	Scanning electron microscopy
EDAX	Energy dispersive
SAED	Selected area electron diffraction
BET	Brunauer Emmett Teller
ZOI	Zone of Inhibition
ROS	Reactive Oxygen Species
DNA	Deoxyribonucleic Acid
MB	Methylene blue
k_{app}	rate constant

References

1. Aashima, Shivani Uppal, Arushi Arora, Sanjeev Gautam, Suman Singh, Choudhary R. J and Mehta S. K. Magnetically retrievable Ce-doped Fe_3O_4 nanoparticles as scaffolds for the removal of azo dyes. RSC Adv., 2019, 9, 23129. DOI: 10.1039/c9ra03252e.
2. Aftabtalab, A and Sadabadi, H., "Application of magnetite (Fe_3O_4) nanoparticles in hexavalent chromium adsorption from aquatic solutions", Journal of Petroleum & Environmental Biotechnology, Vol. 6, No. 200, (2015), 1–6.
3. Agnihotri, P., Lad, V.N., 2020. Magnetic nanofluid: synthesis and characterization. Chem. Pap. 74, 3089–3100. https://doi.org/10.1007/s11696-020-01138-w.
4. Agusu, L., Alimin, Ahmad, L. O., Firihu, M. Z., Mitsudo, S., and Kikuchi, H. (2019). Crystal and Microstructure of $MnFe_2O_4$ Synthesized by Ceramic Method Using Manganese Ore and Iron Sand as Raw Material. Journal of Physics, 1-8.
5. Al-Farhan, B. S., "Removal of Cd and Pb Ions from Aqueous Solutions Using Bentonite-Modified Magnetic Nanoparticles", International Journal of Nano Dimension, Vol. 2, No. 1, (2016), 27–31.
6. Amara D., Felner I., Nowik I., Margel S., Synthesis and characterization of Fe and Fe_3O_4 nanoparticles by thermal decomposition of triiron dodecacarbony, Colloids Surf., A 339 (2009) 106-110.
7. Ancy, K., Vijilvani, C., Bindhu, M.R., Jeslin Sunitha Bai, S., Khalid, S.A., Turki, M.D., Ayman, M., Mohammed, S.A., 2021. Visible light assisted photocatalytic degradation of commercial dyes and waste water by Sn–F co-doped titanium dioxide nanoparticles with potentialantimicrobialapplication.Chemosphere,277, 130247. https://doi.org/10.1016/j.chemosphere.2021.130247.
8. Anjana P. M., Joe Sherin J. F., Vijayakumar C., Sarath Kumar S. R., Bindhu M. R., Rakhi R. B., Mater. Sci. Eng. B 2023, 290, 116313.
9. Anjana, P.M., Bindhu, M.R., Umadevi, M., Rakhi, R.B., 2018. Antimicrobial, electrochemical and photo catalytic activities of Zn doped Fe_3O_4 nanoparticles. J. Mater. Sci. Mater. Elect. 29, 6040-6050. https://doi.org/10.1007/s10854-018- 8578-2.
10. Arakha, M., Pal, S., Samantarrai, D., Panigrahi, T.K., Mallick, B.C., Pramanik, K., Mallick, B.,Jha, S., 2015. Antimicrobial activity of iron oxide nanoparticle upon modulation of nanoparticle-bacteria interface. Sci. Rep. 5(1), 14813. https://doi.org/10.1038/srep14813.
11. Arefeh Ahadi, Hassan Alamgholiloo, Sadegh Rostamnia, Xiao Liu, Mohammadreza Shokouhimehr, Diego A. Alonso, Rafael Luque, Layer-Wise Titania Growth Within Dimeric Organic Functional Group Viologen Periodic Mesoporous Organosilica as Efficient Photocatalyst for Oxidative Formic Acid Decomposition. The European Soceity Journal for Catalysis, 2019. 11(19) p. 4803-4809. https://doi.org/10.1002/cctc.201900486.
12. Asha, S., Hentry, C., Bindhu, M.R., Al-Mohaimeed, A.M., AbdelGawwad, M.R., Elshikh, M.S., 2021. Improved photocatalytic activity for degradation of textile dyeing waste water and thiazine dyes using $PbWO_4$ nanoparticles synthesized by coprecipitation method. Environ. Res.200,111721. https://doi.org/10.1016/j.envres.2021.111721.
13. Ashraf, M.; Shah, S.S.; Khan, I.; Aziz, M.A.; Ullah, N.; Khan, M.; Adil, S.F.; Liaqat, Z.; Usman, M.; Tremel, W.; et al. A HighPerformance Asymmetric Supercapacitor Based on

Tungsten Oxide Nanoplates and Highly Reduced Graphene Oxide Electrodes. Chem. Eur. J. 2021, in press.

14. Athar, T., 2015. Smart precursors for smart nanoparticles. Emerging Nanotechnologies for Manufacturing (Second Edition). Micro and Nano Tech. 444-538. https://doi.org/10.1016/B978-0-323-28990-0.00017-8.
15. Bala, D. A., Ali, H., Eli, D and Yunana, T. "Optical Properties of Reduced Graphene Oxide on Iron Oxide Nanoparticles", Vol. 3 No. 2, June, 2019, pp 226-231.
16. Balamurugan, J.; Nguyen, T. T.; Aravindan, V.; Kim, N. H.; Lee, J., Flexible Solid-State Asymmetric Supercapacitors Based on Nitrogen-Doped Graphene Encapsulated Ternary Metal-Nitrides with Ultralong Cycle Life. Advanced Functional Materials 2018, 28. http://dx.doi.org/10.1002/adfm.201804663.
17. Balamurugan, J.; Nguyen, T. T.; Aravindan, V.; Kim, N. H.; Lee, S. H.; Lee, J. H., All ternary metal selenide nanostructures for high energy flexible charge storage devices. Nano Energy 2019, 65, 10 https://doi.org/10.1016/j.nanoen.2019.103999.
18. Balamurugan, J.; Thanh, T. D.; Kim, N. H.; Lee, J. H., Facile synthesis of 3D hierarchical Ndoped graphene nanosheet/cobalt encapsulated carbon nanotubes for high energy density asymmetric supercapacitors. Journal of Materials Chemistry A 2016, 4 (24), 9555-9565. https://doi.org/10.1039/C6TA03132C.
19. BehnamNayebi, Kasra Pourrostami Niavol, Behzad Nayebi, Soo Young Kim, Ki Tae Nam, Ho Won Jang, Rajender S. Varma and Mohammadreza Shokouhimehr, Prussian blue-based nanostructured materials: Catalytic applications for environmental remediation and energy conversion. Molecular Catalysis, 2021. 514. p. 111835. https://doi.org/10.1016/j.mcat.2021.111835.
20. Beji, Z., Hanini, A., Smiri, L. S., Gavard, J., Kacem, K., Villain, F., et al. (2010). Magnetic properties of Zn-Substituted $MnFe_2O_4$ Nanoparticles Synthesized in Polyol as Potential Heating Agents for Hyperthermia. Evaluation of Their Toxicity on Endhothelial Cells. Chemistry of Materials, 5420-5429.
21. Bessy, T.C., Bindhu, M.R., Johnson, J., Chen, S.-M., Chen, T.-W., Almaary, K. S., 2022. UV light assisted photocatalytic degradation of textile waste water by Mg0.8- x$ZnxFe_2O_4$ synthesized by combustion method and in-vitro antimicrobial activities. Environ. Res. 111917. https://doi.org/10.1016/j.envres.2021.111917.
22. Bharath, G.; Hai, A.; Kiruthiga, T.; Rambabu, K.; Sabri, M. A.; Park, J.; Choi, M. Y.; Banat, F.; Haija, M. A., Fabrication of Ru–$CoFe_2O_4$/RGO hierarchical nanostructures for high-performance photoelectrodes to reduce hazards Cr(VI) into Cr(III) coupled with anodic oxidation of phenols. Chemosphere 2022, 13443. https://doi.org/10.1016/j.chemosphere.2022.134439.
23. Bindhu, M.R., Willington, T.D., Hatshan, M.R., Chen, S.-M., Chen, T.-W., 2021. Environmental photochemistry with Sn/F simultaneously doped TiO_2 nanoparticles: UV and visible light induced degradation of thiazine dye. Environ. Res. 112108. https://doi.org/10.1016/j.envres.2021.112108.
24. Cabot, A., Puntes, V. F., Shevchenko, E., Yin, Y., Balcells, L., Marcus, M. A., Hughes, S.M., Alivisatos, A.P., 2007. Vacancy Coalescence during Oxidation of Iron Nanoparticles. J. American Chem. Soc. 129(34), 10358-10360. http://doi.org/10.1021/ja072574a.

25. Cao, W., Ma, Y., Zhou, W and Guo, L., "One-pot hydrothermal synthesis of rGO-Fe_3O_4 hybrid nanocomposite for removal of Pb (II) via magnetic separation", Chemical Research in Chinese Universities, Vol. 31, No. 4, (2015), 508–513.
26. Chandra, V., Park, J., Chun, Y., Lee, J.W., Hwang, I.C., Kim, K.S., 2010. Waterdispersible magnetite- reduced graphene oxide composites for arsenic removal. ACS Nano 4, 3979e3986. http://dx.doi.org/10.1021/nn1008897.
27. Chang Y. C and Chen D. H., J. Colloid Interface Sci., 283, 446-451 (2005).
28. Chang Y., Li J., Wang B., Luo H., He H., Song Q., and Zhi L. (2013). the creation of 3D nitrogen-doped graphene/Fe3O4 by a metal ion induced self-assembly process for high-performance Li-ion batteries. J. Mater. Chem. A, 1(46), 14658-14665. http://doi.org/10.1039/c3ta13370b.
29. Chen D. Y., Ji G., Ma Y., Lee J. Y., Lu J. M., ACS Appl. Mater. Interfaces 2011, 3, 3078.
30. Chen H. I and Chang H. Y.: Colloid Surface A, 2005, 242, 61-69.
31. Chen, R., Chen, R., Chai, L., Li, Q., Shi, Y., Wang, Y., Mohammad, A., 2013. Preparation and characterization of magnetic Fe_3O_4/CNT nanoparticles by RPO method to enhance the efficient removal of Cr(VI). Environ. Sci. Pollut. Res. Int. 20(10), 7175-85. http://doi.org/10.1007/s11356-013-1671-4.
32. Chen, Y., Fu, X.-Y., Yue, Y.-Y., Zhang, N., Feng, J., Sun, H.-B., 2019. Flexible and transparent supercapacitor based on ultrathin Au/graphene composite electrodes. Applied Surface Sci. 467-468 104-111. http://doi.org/:10.1016/j.apsusc.2018.10.093.
33. Cheng Q. D., Gong S., Zhang Q., Wang R., Jiang L., J. Mater. Chem. A 2017, 5, 16386.
34. Chimezie, A.B., Hajian, R., Yusof, N.A., Woi, P.M. and Shams, N., "Fabrication of reduced graphene oxide-magnetic nanocomposite (rGO-Fe_3O_4) as an electrochemical sensor for trace determination of As (III) in water resources", Journal of Electroanalytical Chemistry, Vol. 796, (2017), 33–42.
35. Chin, A.B., Yaacob, I.I., 2007. Synthesis and characterization of magnetic iron oxide nanoparticles via w/o microemulsion and Massart's procedure. J. Mater. Processing Tech. 191(1), 235-237. https://doi.org/10.1016/j.jmatprotec.2007.03.011.
36. Chou, C. Y.; Kuo, P.C.; Yao, Y.D.; Sun, A. C.; Fang, Y.H.; Chen, S. C.; Huang, C. H.; Chen, J. W. Effects of Sintering Temperature on the Magnetoresistance and Microstructure of the Mixture of Fe_3O_4 and Cu-Ferrite Powder. IEEE Trans. Magn. 2005, 41, 2757-2759.
37. Cruz, I. F., Freire, C., Araújo, J. P., Pereira, C., Pereira, A. M., 2018. Multifunctional Ferrite Nanoparticles: From Current Trends Toward the Future. Magnetic Nanostructured Mater. 59-116. http://doi.org/10.1016/b978-0-12-813904-2.00003-6.
38. Cui, H., Yang, W., Li, X., Zhao, H and Yuan, Z., "An electrochemical sensor based on a magnetic Fe_3O_4 nanoparticles and gold nanoparticles modified electrode for sensitive determination of trace amounts of arsenic (III)", Analytical Methods, Vol. 4, No. 12, (2012), 4176–4181.
39. Cunqing Ma, Kaiyu yang, Lili Wang, Xin Wang. Facile synthesis of reduced graphene oxide/Fe_3O_4 nanocomposite film. J Appl Biomater Funct Mater 2017; 15(Suppl 1):S1-S6. DOI: 10.5301/jabfm.5000341.
40. Deng H., Li X. L., Peng Q., Wang X., Chen J. P., Li Y. D., Monodisperse magnetic single-crystal ferrite microspheres, Angew. Chem. Int. Ed. 44 (2005) 2782-2785.

41. Dubus S., Gravel J. F., Drogoff B. L., Nobert P., Veres T and Boudreau D., Anal. Chem., 78, 4457-4464 (2006).
42. Ferraz I. S. B., Castro T. J., Mantilla J., Coaquira J. A. H., Garg V. K., Oliveira A. C., Franco Jr A., Morais P. C., da Silva S. W., J. Alloys Compd. 2021, 887, 161398.
43. Gade N.E., Dar R.M., Mishra O.P., Khan J.R., Kumar V., and Patyal A.: Evaluation of dose-dependent cytotoxic effects of graphene oxide-iron oxide nanocomposite on caprine Wharton's jelly derived mesenchymal stem cells. J. Anim. Res. 5, 415 (2015).
44. Gautam, S., Shandilya, P., Priya, B., Singh, V. P., Raizada, P., Rai, R., et al. (2017). Superparamagnetic $MnFe_2O_4$ Dispersed over Graphitic Carbon Sand Composite and Bentonite as Magnetically Recoverable Photocatalyst for Antibiotic Mineralization. Seperation and Purification Technology, 498-511.
45. Geim A.K., Novoselov, K.S. 2007. The rise of graphene. Nature Mater.6, 183-191.
46. Gholinejad, M.; Bahrami, M.; Nájera, C. A fluorescence active catalyst support comprising carbon quantum dots and magnesium oxide doping for stabilization of palladium nanoparticles: Application as a recoverable catalyst for Suzuki reaction in water. Mol. Catal. 2017, 433, 12–19.
47. Giraldo, L., Erto, A and Moreno-Piraján, J. C., "Magnetite nanoparticles for removal of heavy metals from aqueous solutions: synthesis and characterization", Adsorption, Vol. 19, No. 2–4, (2013), 465–474.
48. Gupta, S.S., Sreeprasad, T.S., Maliyekkal, S.M., Das, S.K., Pradeep, T., 2012. Graphene from sugar and its application in water purification. ACS Appl. Mater. Interfaces 4156e4163. http://dx.doi.org/10.1021/am300889u.
49. Gurunathan S., Woong Han J., Eppakayala V., and Kim J.: Green synthesis of graphene and its cytotoxic effects in human breast cancer cells. Int. J. Nanomed. 8, 1015 (2013).
50. Han, Q., Wang, Z., Xia, J., Chen, S., Zhang, X., Ding, M., Talanta 2012, 101, 388–395.
51. Hastak V., Bandi S., Kashyap S., Singh S., Luqman S., Lodhe M., Peshwe D.R., and Srivastav A.K.: Antioxidant efficacy of chitosan/ graphene functionalized superparamagnetic iron oxide nanoparticles. J. Mater. Sci.: Mater. Med. 29, 154 (2018).
52. Haw, C.Y., Chia, C.H., Zakaria, S., Mohamed, F., Radiman, S., Teh, C.H., Khiew P.S., Chiu W.S., Huang, N.M., 2011. Morphological studies of randomized dispersion magnetite nanoclusters coated with silica. Ceramint. 37(2), 451-464. http://doi.org/10.1016/j.ceramint.2010.09.010.
53. He, Z.; Koza, J. A.; Mu, G. J.; Miller, A. S.; Bohannan, E. w.; switzer, J. A. Electrodeposition of $Co_xFe_{3-x}O_4$ Epitaxial Films and Superlattices. Chem. Mater. 2013, 25, 223-232.
54. Hisatomi, T., Kubota, J., Domen, K., 2014. Recent advances in semiconductors for photocatalytic and photoelectrochemical water splitting. Chem. Soc. Rev. 43(22), 7520–7535. http://doi.org/10.1039/c3cs60378d.
55. Hoffmann, M.R., Martin, S.T., Choi, W., Bahnemann, D.W., 1995. Environmental Applications of Semiconductor Photocatalysis. Chem. Rev. 95(1), 69– 96. http://doi.org/10.1021/cr00033a004.
56. Hong R. Y., Pan T. T and Li H. Z., J. Magn. Magn. Mater., 303, 60-68 (2006).

57. Hosseini, S.H., Asadnia, A., 2013. Polyaniline/Fe_3O_4 coated on $MnFe_2O_4$ nanocomposite: Preparation, characterization, and applications in microwave absorption. J. Inter. Physical Sci. 8(22), 1209-1217. http://doi.org/10.5897/IJPS12.576.
58. Hu C. Q., Gao Z. H and Yang X. R., Chem. Phys. Lett., 429, 513-517 (2006).
59. Hu F. Q., Li Z., Tu C. F and Gao M. Y., J. Colloid Interface Sci., 311 (2007)469-474.
60. Jalil, Z., Rahwanto, A., Mustanir, Akhyar and Handoko, E. (2017). Magnetic Behaviour of Natural Magnetite (Fe3O4) Extracted from Beach Sand Obtained by Mechanical Alloying Method. AIP Conference Proceeding 1862 (pp. 030023-1-030023-4). Depok: AIP Publishing.
61. Jedrzejczak-Silicka M.: Cytotoxicity and genotoxicity of GO– Fe_3O_4 hybrid in cultured mammalian cells. Pol. J. Chem. Technol. 19, 27 (2017).
62. Jeong D-W, Jang W-J, Shim J-O, Roh H-S. High temperature water–gas shift without pre-reduction over spinel ferrite catalysts synthesized by glycine assisted sol–gel combustion method. Int J Hydrogen Energy 2016;41(6):3870–6.
63. Joe Sherin J. F., Vijayakumar C., Bindhu M. R., Mansour K. Gatasheh, Ashraf Atef Hatamleh and Selvaraj Arokiyara, Phys. Status Solidi A 2023, 220, 2300076.
64. Karim, M. R.; Mohammad, A.; Cho, M. H.; Yoon, T., Synergistic performance of Fe_3O_4/SnO_2/rGO nanocomposite for supercapacitor and visible light-responsive photocatalysis. International Journal of Energy Research 2022, 46 (5), 65 https://doi.org/10.1002/er.7588.
65. Keiser, J.T., Brown, C.W., Heidersbach, R.H., 1982. The Electrochemical Reduction of Rust Films on Weathering Steel Surfaces. J. Electrochem. Soc. 129(12), 2686. http://doi.org/10.1149/1.2123648.
66. Kexin Fang, Lei Shi, Lizhu Yao, Lishuang Cui. Synthesis of novel magnetically separable $Fe_3O_4/Bi_{12}O_{17}C_{l2}$ photocatalyst with boosted visible-light photocatalytic activity. 129(2020)110888.
67. Kim E. H., Lee H. S., Kwak B. K and Kim B. K., J. Magn. Mater., 289, 328-330 (2005).
68. Kim, D. H., Nikles, D.E., and Brazel, C. S. (2010). Synthesis and Characterization of Multifunctional Chitosan-$MnFe_2O_4$ Nanoparticles for Magnetic Hyperthermia and Drug Delivery. Materials, 4051-4065.
69. Kumar P., Huo P., Zhang R., Liu B., Nanomaterials 2019, 9, 737
70. Lassoued A., Lassoued M. S., García-Granda S., Dkhil B., Ammar S., Gadri A., J. Mater. Sci. 2018, 29, 5726
71. Laurent S., Forge D., Port M., Roch A., Robic C., Vander Elst L., Muller R.N., Magnetic iron oxide nanoparticles: synthesis, stabilization, vectorization, physico-chemical characterizations, and biological applications, Chem. Rev. 108 (2008) 2064-2011.
72. Laurent, S.; Forge, D.; Port, M.; Roch, A.; Robic, C.; Elst, L. V.; Muller, R. N. Chem. Rev. 2008, 108, 2064.
73. Lazarevic, Z. Z., Jovalekic, C., Milutinovic, A., Sekulic, D., Ivanoski, V. N., and Recnik, A. (2013). Nanodimensional Spinel $NiFe_2O_4$ and $ZnFe_2O_4$ Ferrites Prepared by soft Mechanochemical Synthesis. Journal of Applied Physics, 1-11.
74. Lee J W, Kim J D. In Situ Chemical Synthesis of Fe_3O_4 Nanoparticles on Reduced Graphene Oxide Sheets in Polyol Medium and Magnetic Properties[J]. Journal of nanoscience and nanotechnology, 2015, 15/1: 215-219.

75. Li Y. X., Zhou X. Z., Wang Y and You X.Z.: Mater. Lett., 2004, 58, 245-249.
76. Lian P. C., Zhu X. F., Xiang H. F., Li Z., Yang W. S., Wang H. H., Electrochim. Acta 2010, 56, 834.
77. Liang JJ, Xu YF, Sui D, et al. Flexible, magnetic and electrically conductive graphene/Fe_3O_4 paper and its application for magnetic controlled switches. J Phys Chem C. 2010;114(41):17465-17471.
78. Liang, C., Song, J., Zhang, Y., Guo, Y., Deng, M., Gao, W., Zhang, J., 2020. Facile Approach to Prepare rGO@Fe_3O_4 Microspheres for the Magnetically Targeted and NIRresponsive Chemo-photothermal Combination Therapy. Nanoscale Res. Lett. 15(1), 86. http://doi.org/10.1186/s11671-020-03320-1.
79. Lin, L., Liu, Y., Zhao, X., Li, J. H., Anal. Chem. 2011, 83, 8396-8402.
80. Liu MM, Sun J. In situ growth of monodisperse Fe_3O_4 nanoparticles on graphene as flexible paper for supercapacitor. Journal of Materials Chemistry A. 2014;2(30):12068-12074.
81. Liu, L.; Zhu, X.; Zeng, Y.; Wang, H.; Lu, Y.; Zhang, J.; Yin, Z.-Z.; Chen, Z.; Yang, Y.; Li, L., An Electrochemical Sensor for Diphenylamine Detection Based on Reduced Graphene Oxide/Fe3O4-Molecularly Imprinted Polymer with 1,4-Butanediyl-3,3'- bis-l-vinylimidazolium Dihexafluorophosphate Ionic Liquid as Cross-Linker. Polymers 2018, 10, 13. http://dx.doi.org/10.3390/polym10121329.
82. Liu, S.; Yu, B.; Wang, S.; Shen, Y.; Cong, H., Preparation, surface functionalization and application of Fe_3O_4 magnetic nanoparticles. Advances in Colloid and Interface Science 2020, 281, 10216. https://doi.org/10.1016/j.cis.2020.102165.
83. Liu, Y.; Wang, W.; Xu, X.; Marcel Veder, J.-P.; Shao, Z., Recent advances in anion-doped metal oxides for catalytic applications. Journal of Materials Chemistry A 2019, 7 (13), 7280-7300. https://doi.org/10.1039/C8TA09913H.
84. Lu, A.-H.; Salabas, E. L.; Schuth, F. Angew. Chem., Int. Ed. 2007, 46, 1222.
85. Lyubutin, I.S., Baskakov, A.O., Starchikov, S.S., Shih, K.-Y., Lin, C.-R., Tseng, Y.-T., Yang, S.-S., Han, Z.-Y., Ogarkova, Yu.L., Nikolaichik, V.I., Avilov, A.S., 2018. Synthesis and characterization of graphene modified by iron oxide nanoparticles. Mater. Chem. Phy. 219, 411-420. http://doi.org/10.1016/j.matchemphys.2018.08.042.
86. Mahalingam, S and Ahn, Y. H., "Improved visible light photocatalytic activity of rGO–Fe_3O_4–NiO hybrid nanocomposites synthesized by in situ facile method for industrial wastewater treatment applications", New Journal of Chemistry, Vol. 42, No. 6, (2018), 4372–4383.
87. Mahdavi M., Namvar F., Ahmad M. B and Mohamad R., Molecules, 18, 5954(2013) DOI: 10.3390/molecules 18055954.
88. Mahdavi M., Namvar F., Ahmad M. B and Mohamad R., Molecules, 18, 5954(2013) DOI: 10.3390/molecules 18055954.
89. Maity, D., Agrawal, D.C., 2007. Synthesis of iron oxide nanoparticles under oxidizing environment and their stabilization in aqueous and non-aqueous media. J. Magnetism and Magnetic Mater. 308(1), 46-55. http://doi.org/10.1016/j.jmmm.2006.05.001.
90. Mandal, P., Chattopadhyay, A.P., 2015. Excellent catalytic activity of magnetically recoverable Fe_3O_4–graphene oxide nanocomposites prepared by a simple method. Dalton Trans. 44(25), 11444-11456. http://doi.org/10.1039/c5dt01260k.

91. Manikandan A., Vijaya J. J., Mary J. A., Kennedy L. J., Dinesh A., J. Ind. Eng. Chem. 2014, 20, 2077.
92. Matijevic E., sapieszko R.S., Melville J.B., Ferric hydrous oxide sols I. Monodispersed basic iron(III) sulfate particles, J. Colloid Interface Sci. 50 (1975) 567-581.
93. Mishra, A., Mohanty, T., 2016. Structural and morphological study of magnetic Fe_3O_4/ reduced graphene oxide nanocomposites. Materials Today: Proceedings 3(6), 1576-1581. https://doi.org/10.1016/j.matpr.2016.04.045.
94. Modwi A., Khezami L., Taha K. K., Bessadok A., Mokraoui S., J. Mater. Sci. Mater. Electron. 2019, 30, 14714.
95. Moradinasab, S and Behzad, M., "Removal of heavy metals from aqueous solution using Fe_3O_4 nanoparticles coated with Schiff base ligand", Desalination and Water Treatment, Vol. 57, No. 9, (2016), 4028–4036.
96. Moyer, J. A.; Vaz, C. A. F.; Negusse, E.; Arena, D. A.; Henrich, V. E. Controlling the Electronic Structure of Co_{1-x} $Fe_{2+x}O_4$ Thin Films through Iron Doping. Phys. Rev. B 2011, 83, 035121.
97. Mussa, Y.; Ahmed, F.; Arsalan, M.; Alsharaeh, E. Two dimensional (2D) reduced graphene oxide (RGO)/hexagonal boron nitride (h-BN) based nanocomposites as anodes for high temperature rechargeable lithium-ion batteries. Sci. Rep. 2020, 10(1), 1-13, https://doi.org/10.1038/s41598-020-58439-z.
98. Naderi F, Nayebzadeh H. Performance and stability assessment of Mg-Al-Fe nanocatalyst in the transesterification of sunflower oil: Effect of Al/Fe molar ratio. Ind Crops Prod 2019;141:111814.
99. Namvari, M and Namazi, H., "Clicking graphene oxide and Fe_3O_4 nanoparticles together: an efficient adsorbent to remove dyes from aqueous solutions", International Journal of Environmental Science and Technology, Vol. 11, No. 6, (2014), 1527–1536.
100. Naseri, M. G., Saion, E. B., Ahangar, H. A., Hashim, M., and Shaari, A. H. (2011). Synthesis and Characterization of Manganese Ferrite Nanoparticles by Thermal Treatment Method. Journal of Magnetism and Magnetic Material, 1745- 1749.
101. Nayamadi Mahmoodabadi A., Kompany A., Mashreghi M., Mater. Chem. Phys. 2018, 213, 285.
102. Ng, W.C., Tan C.Y., Ong, B.H., Matsuda, A. Procedia Eng., 2017, 184, 587-594.
103. Novoselov K. S., Geim A. K., Morozov S. V., Jiang D., Zhang Y., Dubonos S. V., Grigorieva I. V., Firsov A. A., Science 2004, 306, 666.
104. Ou J, Wang F, Huang Y, et al. Fabrication and cyto-compatibility of Fe_3O_4/SiO_2/graphene-CdTe QDs/CS nanocomposites for drug delivery. Colloids Surf B Biointerfaces. 2014;117:466-472.
105. Padhi, D.K., Panigrahi, T.K., Parida, K., Singh, S.K. and Mishra, P. M., "Green synthesis of Fe_3O_4/RGO nanocomposite with enhanced photocatalytic performance for Cr (VI) reduction, phenol degradation, and antibacterial activity", ACS Sustainable Chemistry & Engineering, Vol. 5, No. 11, (2017), 10551–10562.
106. Peik-See, T., Pandikumar, A., Ngee, L.H., Ming, H.N. and Hua, C. C., "Magnetically separable reduced graphene oxide/iron oxide nanocomposite materials for environmental remediation", Catalysis Science & Technology, Vol. 4, No. 12, (2014), 4396– 4405.

107. Pelin M., Fusco L., León V., Martín C., Criado A., Sosa S., Vázquez E., Tubaro A., and Prato M.: Differential cytotoxic effects of graphene and graphene oxide on skin keratinocytes. Sci. Rep. 7, 1 (2017).
108. Penc B., Hofmann M., Slaski M., Starowicz P and Szytula A.: J. Alloy. Compd. 1999, 282, 8-13.
109. Perreault F., De Faria A.F., Nejati S., and Elimelech M.: Antimicrobial properties of graphene oxide nanosheets: Why size matters. ACS Nano 9, 7226 (2015).
110. Qiao, R; Yang, C.; Gao, M. J. Mater, Chem. 2009, 19, 6274.
111. Qin S., Xiao W., Zhou C., Pu Q., Deng X., Lan L., Liang H., Song X., Wu M., Signal Trans. Target Ther. 2022, 7, 199.
112. Rahmani Vahid B, Haghighi M. Urea-nitrate combustion synthesis of MgO/$MgAl_2O_4$ nanocatalyst used in biodiesel production from sunflower oil: Influence of fuel ratio on catalytic properties and performance. Energy Convers Manage 2016;126:362–72.
113. Ramanathan, S.; SasiKumar, M.; Radhika, N.; Obadiah, A.; Durairaj, A.; Helen Swetha, G.; Santhoshkumar, P.; Sharmila Lydia, I.; Vasanthkumar, S., Musa paradisiaca reduced graphene oxide (BRGO) /MWCNT-Fe_3O_4 nanocomposite for supercapacitor and photocatalytic applications. Materials Today: Proceedings 2021, 47, 843-85. https://doi.org/10.1016/j.matpr.2021.01.706.
114. Rezapour, M., 2018. One-step electrochemical synthesis and characterization of high performance magnetite/reduced graphene oxide nanocomposite. Anal. Bioanal. Electrochem. 10, 450-464.
115. Riana, M., Sembiring, T., Situmorang, M. Kurniawan, C., Setiadi, E. A., Tetuko, A. P., et al. (2018). Preparation and Characterization of Natural Iron Sand from Kata Beach, Sumatera Barat Indonesia with High Energy Milling (HEM). Jurnal Natural, 97-100.
116. Ribeiro M., Monteiro F. J., Ferraz M. P., Biomatter 2012, 2, 176.
117. Santos C.M., Mangadlao J., Ahmed F., Leon A., Advincula R.C., and Rodrigues D.F.: Graphene nanocomposite for biomedical applications: Fabrication, antimicrobial and cytotoxic investigations. Nanotechnology 23, 395101 (2012).
118. Setiadi, E. A., Yunus, M., Nababan, N., Simbolon, S., Kurniawan, C., Humaidi, S., et al. (2017). The Effect of Temperature on Synthesis of $MgFe_2O_4$ Based on Natural Iron Sand by Co-precipitation Method as Adsorbent Pb Ion. Journal of Physics: Conference Series, Vol. 985, pp.012046.
119. Sharma, N., Sharma, V., Jain, Y., Kumari, M., Gupta, R., Sharma, S. K., Sachdev, K., 2017. Synthesis and Characterization of Graphene Oxide (GO) and Reduced Graphene Oxide (rGO) for Gas Sensing Application. Macromol. Symp. 376(1), 1700006. http://doi.org/10.1002/masy.201700006.
120. Sharma, N; Sharma, V; Sharma, S.K; Sachdev, K. Synthesis and Characterization of Graphene Oxide (GO) and Reduced Graphene Oxide (rGO) for Gas Sensing Application. Macromol. Symp. 2017, 376, 1700006. DOI: 10.1002/masy.201700006.
121. Simeonidis K., Mourdikoudis S., Moulla M., et al., J. Magnetism and Magnetic Materials., 316(2), e1(2007), DOI: 10.1016/j.jmmm.2008.01.028.
122. Somvanshi, S.B., Khedkar, M.V., Kharat, P.B., Jadhav, K.M., 2020. Influential diamagnetic magnesium (Mg^{2+}) ion substitution in nano-spinel zinc ferrite ($ZnFe_2O_4$):

Thermal, structural, spectral, optical and physisorption analysis. Ceramint. 46(7), 8640-8650. http://doi.org/10.1016/j.ceramint.2019.12.097

123. Su shiung Lam, Van-Huy Nguyen, Minh Tuan Nguyen Dinh, Dinh Quang Khieu, Duc Duong La, Huu Trung Nguyen, Dai Viet N. Vo, Changlei Xia, Rajender S. Varma, Mohammadreza, Shokouhimehr, Chinh Chien Nguyen, Quyet Van Le and Wanxi Peng, Mainstream avenues for boosting graphitic carbon nitride efficiency: towards enhanced solar light-driven photocatalytic hydrogen production and environmental remediation. Journal of Materials Chemistry A, 2020. 8(21) p. 10571-10603. https://doi.org/10.1039/D0TA02582H.

124. Sun, J., Zhou, S., Hou, P., Yang, Y., Weng, J., Li, X., Li, M., 2006. Synthesis and characterization of biocompatible Fe3O4 nanoparticles. J. Biomed. Mater. Res. A, 80(2), 333-41. http://doi.org/10.1002/jbm.a.30909.

125. Sun, X.J., Liu, F.T., Jiang, Q.H., 2011. Synthesis and Characterization of Co^{2+} -Doped Fe_3O_4 Nanoparticles by the Solvothermal Method. Mater. Sci. Forum 688, 364-369. http://doi.org/10.4028/www.scientific.net/msf.688.364.

126. Sun, Y.F., Chen, W.K., Li, W.J., Jiang, T.J., Liu, J.H and Liu, Z. G., "Selective detection toward Cd^{2+} using Fe_3O_4/RGO nanoparticle modified glassy carbon electrode", Journal of Electroanalytical Chemistry, Vol. 714, (2014), 97–102.

127. Takaobushi, J.; et al. Electronic Structures of $Fe_{(3-x)}M_{(x)}O_{(4)}$ (M=Mn, Zn) Spinel Oxide Thin Films Investigated by X-Ray Photo emission Spectroscopy and X-Ray Magnetic Circular Dichroism. Phys. Rev. B 2007, 76, 205108.

128. Tang N.J., Zhong W., Jiang H.Y., Nanostructured magnetite (Fe_3O_4) thin films prepared by sol-gel method, J. Magn. Magn. Mater.282(2004) 92-95.

129. Tang, L. H., Wang, Y., Li, Y. M., Feng, H. B., Lu, J., Li, J. H., Adv. Funct. Mater. 2009, 19, 2782–2789.

130. Tripathy, D.; Adeyeye, A. O. ; Boothroyd, C. B.; Piramanayagam, S. N. Magnetic and Transport Properties of Co-Doped Fe_3O_4 Films. J. Appl. Phys. 2007, 101, 013904.

131. Tsai M. S.: Mat. Sci. Eng. B, 2004, 110, 132-134.

132. Van-HuyNguyen, Ba-Son Nguyen, Zhong Jin, Mohammadreza, Shokouhimehr, Ho Won Jang, Chechia Hu, Pardeep Singh, Pankaj Raizada, Wanxi Peng, Su Shiung Lam, Changlei Xia, Chinh Chien Nguyen, Soo Young Kim and Quyet Van Le, Towards artificial photosynthesis: Sustainable hydrogen utilization for photocatalytic reduction of CO_2 to high-value renewable fuels. Journal of Chemical Engineering, 2020. 402. p. 126184. https://doi.org/10.1016/j.cej.2020.126184.

133. Vermisoglou, E.C., Jakubec, P., Bakandritsos, A., Pykal, M., Talande, S., Kupka, V., Zboril, R., Otyepka, M. Chemical Tuning of Specific Capacitance in Functionalized Fluorographene. Chem. Matter., 2019, 31(13), 4698-4709.

134. Wang F, Chen D, Zhang N, Wang S, Qin L, Sun X, et al. Oxygen vacancies induced by zirconium doping in bismuth ferrite nanoparticles for enhanced photocatalytic performance. J Colloid Interface Sci 2017;508:237–47.

135. Wang, H., Yuan, X., Wu, Y., Chen, X., Leng, L., Wang, H., Li, H and Zeng, G., "Facile synthesis of polypyrrole decorated reduced graphene oxide–Fe_3O_4 magnetic composites and its application for the Cr (VI) removal", Chemical Engineering Journal, Vol. 262, (2015), 597–606.

136. Wang, J., Tang, B., Tsuzuki, T., Liu, Q., Hou, X. & Sun, L. 2012. Synthesis, characterization and adsorption properties of superparamagnetic polystyrene/Fe_3O_4/graphene oxide. Chem. Eng. J. 204, 258–263.

137. Wang, W.P., Yang, H., Xian, T., Jiang, J.L., 2012. XPS and Magnetic Properties of $CoFe_2O_4$ Nanoparticles Synthesized by a Polyacrylamide Gel Route. Mater.Trans. 53(9), 1586-1589. http:// doi.org/10.2320/matertrans.m2012151.

138. Wang, X. L., Bai, H., Jia, Y. Y., Zhi, L. J., Qu, L. T., Xu, Y. X., Li, C., Shi, G. Q., RSC Adv. 2012, 2, 2154–2160.

139. Wang, X. L., Bai, H., Yao, Z. Y., Liu, A. R., Shi, G. Q., J. Mater. Chem. 2010, 20, 9032–9036.

140. Wang, Y., Li, Z. H., Hu, D. H., Lin, C. T., Li, J. H., Lin,Y. H., J. Am. Chem. Soc. 2010, 132, 9274-9276.

141. Wang, Y., Shao, Y. Y., Matson, D. W., Li, J. H., Lin, Y. H., ACS Nano 2010, 4, 1790–1798.

142. Wang, Z. H., Xia, J. F., Zhu, L. Y., Chen, X. Y., Zhang, F. F., Yao, S. Y., Li, Y. H., Xia Y. Z., Electroanalysis 2012, 23, 2463–2471.

143. Wang, Z. H., Xia, J. F., Zhu, L. Y., Zhang, F. F., Guo, X. M., Li, Y. H., Xia, Y. Z., Sens. Actuators B: Chem. 2012, 161, 131–136.

144. Wu Z. Y., Xu X. X., Hu B. C., Liang H. W., Lin Y., Chen L. F., Yu S. H., Angew. Chem. 2015, 54, 8179.

145. Wu, Q.; Xu, Y.; Yao, Z.; Liu, A.; Shi, G. Supercapacitors based on flexible graphene/polyaniline nanofiber composite films. ACS Nano 2010, 4, 1963–1970.

146. Xu Z. C., Shen C.M., Hou Y.L., Gao H.J., Sun S.H., Oleylamine as both reducing agent and stabilizer in a facile synthesis of magnetite nanoparticles, Chem. Mater.21 (2009) 1778-1780.

147. Yadav, R. S., Kuritka, I., Vilcakova, J., Masilko, J., Kalina, L., et al. (2017). Structural, Magnetic, Dielectric and Electric Properties ov $NiFe_2O_4$ Spinel Ferrite Nanoparticles Prepared by Honey- Mediated Sol-Gel Combustion. Journal of Physical and Chemistry of Solids, 1-42.

148. Yang W., Ratinac K. R., Ringer S. P., Thordarson P., Gooding J. J., Braet F., Angew. Chem. Int. Ed. 2010, 49, 2114.

149. Yang X., Zhang X., Ma Y., Huang Y., Wang Y., Chen Y., Superparamagnetic graphene oxide–Fe_3O_4nanoparticles hybrid for controlled targeted drug carriers, J. Mater. Chem. 19 (18) (2009) 2710–2714, https://doi.org/10.1039/b821416f.

150. Yang Z., Hao X., Chen S., Ma Z., Wang W., Wang C., Yue L., Sun H., Shao Q., Murugadoss V., and Guo Z.: Long-term antibacterial stable reduced graphene oxide nanocomposites loaded with cuprous oxide nanoparticles. J. Colloid Interface Sci. 533, 13 (2019).

151. Yang, H.-M.; Lee, H. J.; Jang, K.-S.; Park, C. W.; Yang, H. W.; Heo, W. D.; Kim, J.-D.J. Mater. Chem. 2009, 19, 4566.

152. Yang, H.-M.; Lee, H. J.; Park, C. W.; Yoon, S. R.; Lim, S.; Jung, B. H.; Kim, J.-D. Chem. Commun. 2011, 47, 5322.

153. Yang, L., Tian, J., Meng, J., Zhao, R., Li, C., Ma, J. and Jin, T., "Modification and characterization of Fe_3O_4 nanoparticles for use in adsorption of alkaloids", Molecules, Vol. 23, No. 3, (2018), 176–185.
154. Yang, S., Zeng, T., Li, Y., Liu, J., Chen, Q., Zhou, J., Ye, Y. and Tang, B., "Preparation of graphene oxide decorated Fe_3O_4@ SiO_2 nanocomposites with superior adsorption capacity and SERS detection for organic dyes", Journal of Nanomaterials, Vol. 16, No. 1, (2015), 1–8.
155. Yao, Y., Miao, S., Liu, S., Ma, L. P., Sun, H. & Wang, S. 2012. Synthesis, characterization, and adsorption properties of magnetic Fe_3O_4:graphene nanocomposite. Chem. Eng. J. 184, 326–332.
156. Yavuz, C.T., Mayo, J.T., Yu, W.W., Prakash, A., Falkner, J.C., Yean, S., Cong, L., Shipley, H.J., Kan, A., Tomson, M., Natelson, D., Colvin, V.L., 2006. Low-Field Magnetic Separation of Monodisperse Fe_3O_4 Nanocrystals. Sci. 314(5801), 964– 967. http://doi.ord/10.1126/science.1131475.
157. Yu, L., Wu, H., Wu, B., Wang, Z., Cao, H., Fu, C. and Jia, N., "Magnetic Fe_3O_4-reduced graphene oxide nanocompositesbased electrochemical biosensing", Nano-Micro Letters, Vol. 6, No. 3, (2014), 258–267.
158. Zhang H, Xie AJ, Wang CP, Wang HS, Shen YH, Tian XY. Room temperature fabrication of an RGO-Fe_3O_4 composite hydrogel and its excellent wave absorption properties. RSC Advances. 2014;4(28):14441-14446.
159. Zhang Y., Yang Y., Dong Z., Shen J., Song Q., Wang X., Mao W., Pu Y., Li X., J. Mater. Sci. Mater. Electron. 2020, 31, 15007.
160. Zhang Z., Dou M., Liu H., Dai L., Wang F., Small 2016, 12, 4193.
161. Zhang, Y., Tang, Y., Li, S., Yu, S., Chem. Eng. J. 2013, 222, 94–100.
162. Zhao G, Mo Z, Zhang P, et al. Synthesis of graphene/ Fe_3O_4/NiO magnetic nanocomposites and its application in photocatalytic degradation the organic pollutants in wastewater[J]. Journal of Porous Materials, 2015, 22/5: 1245-1253.
163. Zhao, G., Song, S., Wang, C., Wu, Q., Wang, Z., Anal. Chim. Acta 2011, 708, 155–159.
164. Zhou GM, Wang DW, Li F, et al. Graphene-wrapped Fe_3O_4 anode material with improved reversible capacity and cyclic stability for lithium ion batteries. Chem Mater. 2010; 22(18): 5306-5313.
165. Zhou W., Tang K., Zeng S., and Qi Y., Nanotechnology, 19(6), (2008), DOI:10.1088/0957- 4484/19/6/065602.